UNIVERSIDAD DE CONCEPCIÓN
FACULTAD DE CIENCIAS FÍSICAS Y MATEMÁTICAS
DEPARTAMENTO DE ASTRONOMÍA

Benchmarking the infrared dark cloud G351.77-0.53: Gaia DR3 distance, mass distribution, and star formation content

Evaluación comparativa de la nube molecular G351.77-0.53: distancia usando Gaia DR3, distribución de masa y contenido de formación estelar

Por: Simón Darío Reyes Reyes

Tesis presentada a la Facultad de Ciencias Físicas y Matemáticas de la Universidad de Concepción para optar al grado académico de Magíster en Astronomía

julio 2023

Concepción, Chile

Profesor Guía: Amelia Marie Stutz

A Ximena, mi madre, por haberme brindado todo el amor para crecer y tener las mejores oportunidades. A mi hermanita Julieta, por llenar de alegría mis días y para que persigas tus sueños. A Juan Carlos y toda mi familia, por el inmenso e incondicional apoyo en todas las etapas de mi vida.

AGRADECIMIENTOS

Agradezco a mi guía de tesis Amelia Stutz, por haber sabido transmitirme metodología para desarrollar ciencia. Agradezco también a Tom Megeath y a quienes formaron parte de esta investigación: Fengwei Xu, Rodrigo Álvarez G., Hong Li Liu y Nicolás Sandoval G. También hicieron posible este trabajo mis amigos del grupo de formación estelar y de la carrera: Cata, Nico, Diego, Rodrigo, Vanessa, Benja, Emilio (QEPD) y todos quienes crearon ese gran ambiente de recreación y amistad. Agradezco a mis queridos amigos de infancia Lucas, Mati y Hugo por estar siempre presentes, y por ser fundamentales para sobrellevar los dos años de encierro. A mis amigos de Geología por acompañarme a crecer como persona: Cami, Edu, Dans, Felipe, y un gran etcétera, incluyendo a quienes me acompañaron por 8 inolvidables temporadas en el equipo de fútbol. Finalmente agradezco inmensamente a mi familia por su inconmesurable cariño y apoyo, a mis siempre atentos abuelitos, mis tíos, primos, la sacrificada y luchadora gran mamá que tengo, Juan Carlos y la Juli. Sin mi familia no estaría persiguiendo lo que más deseo.

Resumen

Presentamos un estudio sobre la actividad global de formación de estrellas en la nube molecular G351.77-0.54 (G351 en adelante). La nube se caracteriza por su estructura filamentosa y opaca al infrarrojo (IR), y por evidenciar formación de un proto- cúmulo de estrellas. Nuestro objetivo es establecer sus propiedades de formación estelar y compararlas con las de otras regiones estándar, como la nube de Orion-A y sus subestructuras. Comenzamos caracterizando sus Objetos Estelares Jóvenes (*YSOs*, por sus siglas en inglés) usando YSOs de archivo e identificando nuevos YSOs. Combinamos estas fuentes con las de Gaia *DR3* y, a partir de los paralajes promedio de miembros probables de la nube, obtenemos una distancia de $\sim 2{,}0 \pm 0{,}15$ kpc, resolviendo la gran ambiguedad en literatura sobre la distancia. Usando nuestro mapa de N(H_2) derivado de Herschel, medimos una masa total de 10200 $M_\odot$ (en un área de 11 pc^2) para el filamento, además de su perfil de masa promediada por unidad de longitud, el cual modelamos como una simple ley de potencia $\lambda = 1585(w/\mathrm{pc})^{0{,}62}\ M_\odot\,\mathrm{pc}^{-1}$, donde w es el radio (projectado en el cielo) del filamento. Nuestro perfil λ es dominado por la emisión del filamento dentro de $w < 0{,}63$ pc, donde tanto el perfil como el índice de potencia de λ son mayores que los de Orion A y sus subestructuras, excepto los del centro del Cúmulo de Orion (para $w \lesssim 0{,}19$ pc). Esto demuestra que G351 contiene un gran reservorio de gas denso, el cual puede potencialmente acelerar su formación de estrellas. A partir de las YSOs vistas en el filamento (dentro de $w < 0{,}63$ pc), estimamos su Eficiencia y Tasa de Formación Estelar (SFE y SFR respectivamente, por sus siglas en inglés), aplicando un factor de 5 para corregir la incompletitud del catálogo de YSOs, calibrado a la distancia de Orion A. Así, la SFE de G351 es $\sim 1{,}8$ veces menor que la de Orion A y menor que la del valor medio de las nubes moleculares locales de la Galaxia. Para diferentes contornos de emisión de N(H_2), medimos SFRs y masas de gas para estimar la Eficiencia por tiempo de *free-fall* ($\varepsilon_{\mathrm{ff}}$) de G351, y verificar leyes de formación propuestas para nubes locales.

Observamos que nuestro $\varepsilon_{\rm ff}$ es 1.1 dex inferior al promedio de dicha ley, y $\sim 4{,}7\times$ inferior al de Orion A. Estas observaciones indican que tal ley de formación estelar no refleja las variaciones presentes en sistemas formadores de estrellas de la Galaxia. Finalmente, especulamos que una acentuada juventud y/o campos magnéticos podrían explicar la ineficiencia para formar estrellas de G351.

Keywords – stars: formation – astrometry – ISM: clouds – submillimetre: ISM

Abstract

While intensively studied, it remains unclear how the star formation (SF) in Infrared Dark Clouds (IRDCs) compares to that of nearby clouds. We study G351.77-0.53 (henceforth G351), a cluster-forming filamentary IRDC. We begin by characterizing its young stellar object (YSO) content. Based on the average parallax of likely members, we obtain a Gaia distance of $\sim 2{,}0 \pm 0{,}15$ kpc, resolving the literature distance ambiguity. Using our Herschel-derived N(H_2) map, we measure a total gas mass of 10200 $M_\odot$ (within 11 pc^2) and the average line-mass profile of the entire filament, which we model as $\lambda = 1585(w/\mathrm{pc})^{0{,}62}\ M_\odot\,\mathrm{pc}^{-1}$. At $w < 0{,}63$ pc, our λ profile is higher and has a steeper power-law index than λ profiles extracted in Orion A and most of its substructures. Based on the YSOs inside the filament area, we estimate the SF efficiency (SFE) and SF rate (SFR). We calculate a factor of 5 incompleteness correction for our YSO catalog relative to Spitzer surveys of Orion A. The G351 SFE is $\sim 1{,}8$ times lower than that of Orion A and lower than the median value for local clouds. We measure SFR and gas masses to estimate the efficiency per free-fall time, $\varepsilon_{\mathrm{ff}}$. We find that $\varepsilon_{\mathrm{ff}}$ is $\sim$1.1 dex below the previously proposed mean local relation, and $\sim 4{,}7\times$ below Orion A. These observations indicate that local SF-relations do not capture variations present in the Galaxy. We speculate that cloud youth and/or magnetic fields might account for the G351 inefficiency.

Keywords – stars: formation – astrometry – ISM: clouds – submillimetre: ISM

Índice general

Índice de cuadros

Índice de figuras

Capítulo 1

Introduction

The identification of mid-infrared dark clouds (IRDC) seen in silhouette against the stars and nebulosity of the galactic plane revealed a population of clouds that potentially contain the earliest stages of cluster and high mass star formation ($M > 8\ M_{\odot}$) (e.g. Egan et al., 1998; Carey et al., 1998; Rathborne et al., 2007; Sanhueza et al., 2012, 2019; Li et al., 2023). Although subsequent studies showed the sample of IRDCs to be heterogeneous and dominated by clouds that will not form high mass stars (Kauffmann and Pillai, 2010), massive IRDCs may form in some cases large clusters of low and high mass stars, as found in the Orion A cloud (Motte et al., 2018; Stutz and Gould, 2016; Megeath et al., 2022). Existing surveys in the visible, IR and submillimiter (sub-mm), now give us the tools needed to compare IRDCs to nearby, star forming, molecular clouds. Via such comparisons, we can better establish the differences between IRDCs and nearby clouds, and establish whether IRDCs are similar to clouds in the nearest 1.5 kpc, or whether they are deficient in star formation. If they are indeed deficient, this would imply they are either in the early stages of star formation or that they have systematically different star formation properties, presumably due to environmental factors (e.g. magnetic fields, turbulence).

Given that low to intermediate mass stars dominate the number of stars formed in

molecular clouds, and given that they – in contrast to high mass stars – form in a wide range of gas environments, low to intermediate mass YSOs provide an excellent tracer of star formation (Megeath et al., 2022). Unlike high mass star formation, which is often accompanied by bright extended mid-IR nebulosity (Motte et al., 2018; Povich et al., 2013), low to intermediate mass YSOs are best identified in point source surveys. Wide field mid-IR imaging with Spitzer and the Wide-field Infrared Survey Explorer (WISE; Wright et al. 2010) provide the means to reliably identify low to intermediate mass YSOs in IRDCs. In particular, the Galactic Legacy Infrared Midplane Survey Extraordinaire (Glimpse) survey (Benjamin et al., 2003; Churchwell et al., 2009) has provided $2''$ angular resolution image of the plane of our galaxy. Built on these surveys, the SPICY catalog uses a machine learning approach to a combination of Glimpse and near-IR surveys to identify protostars (Kuhn et al., 2021b). For an all sky view, Marton et al. (2019) combined the AllWISE (Cutri et al., 2013) and GAIA (Gaia Collaboration et al., 2016, 2022) catalogs to identify YSOs, although with a significantly lower angular resolution ($6''$) and sensitivity compared to Spitzer. From the number of YSOs detected in these surveys, SFRs can be determined for the IRDCs. These can then be compared to the SFRs of nearby clouds without relying on comparatively sparse and poorly characterized high mass stellar populations.

Turning to the gas mass reservoir, which must be characterized in star and cluster forming systems, far-IR and (sub-)millimeter surveys complement these SFRs by mapping the structure of the cold, molecular gas over molecular cloud scales. In particular, the ATLASGAL survey, the Planck Survey, and Herschel Infrared Galactic Plane survey (Hi-GAL, Molinari et al., 2010, 2016) data can be used to make maps of the structure of molecular clouds through their thermal dust emission (e.g., Launhardt et al., 2013; Stutz et al., 2013; Stutz and Kainulainen, 2015; Csengeri et al., 2016; Álvarez-Gutiérrez et al., 2021). These can be compared to maps of nearby clouds using various methods for characterizing filamentary clouds (Stutz and Kainulainen, 2015; Stutz and Gould, 2016). More fundamentally, any mass measurements directly depends

on the distance estimation to these clouds, and here the accurate astrometry of the Gaia survey have been playing a major role during the last decade by providing the means for establishing distances to regions if their embedded members can be found in the Gaia archive.

In combination, the distances, SFRs, and gas column densities can be used to directly compare star formation in IRDCs to that in nearby clouds (Pokhrel et al., 2021; Megeath et al., 2022). Recently, surveys of YSOs of nearby molecular clouds have found a significant degree of uniformity in local clouds (Gutermuth et al., 2011; Lada et al., 2013; Pokhrel et al., 2020; Pokhrel et al., 2021). In particular, Pokhrel et al. (2021) establish a relation where the star formation rate efficiency per local free-fall time ($\varepsilon_{\rm ff}$) is 2.5 % (also see Hu et al. 2021), which is established in a sample of clouds ranging from low mass star forming clouds at 140 pc to high mass star forming clouds at 1.4 kpc. Although still under debate (Lada et al., 2013; Evans et al., 2014), these star formation relations (SF-relations) provide a benchmark for comparing the SFRs in IRDCs to those in nearby clouds.

G351.77-0.53 (henceforth G351) is a filamentary IRDC that has been studied through a series of primarily millimeter observations. Despite the attention, the large uncertainty in the distance, with estimates ranging from 1-2 kpc, results in significant uncertainties in the inferred properties. Previous estimations of the G351 filament are focused on the protocluster area and are based on Galactic rotation curve models. Motte et al. (2022) reported a distance $D = 2$ kpc from the BeSSeL kinematic distance calculator, which is an average between the two equally probable solutions 1.3 and 2.7 kpc retrieved by the calculator. Leurini et al. (2011a) reported a distance $D \leq 1$ kpc using velocities based on thermal lines. Other distances $D = 0.7$, 1, 2.2 kpc are also reported in the literature based on maser emission lines (Forster and Caswell 1989; MacLeod et al. 1998; Norris et al. 1993; Miettinen et al. 2006).

We study two fields in the G351 IRDC. Firstly, a larger scale field that captures the

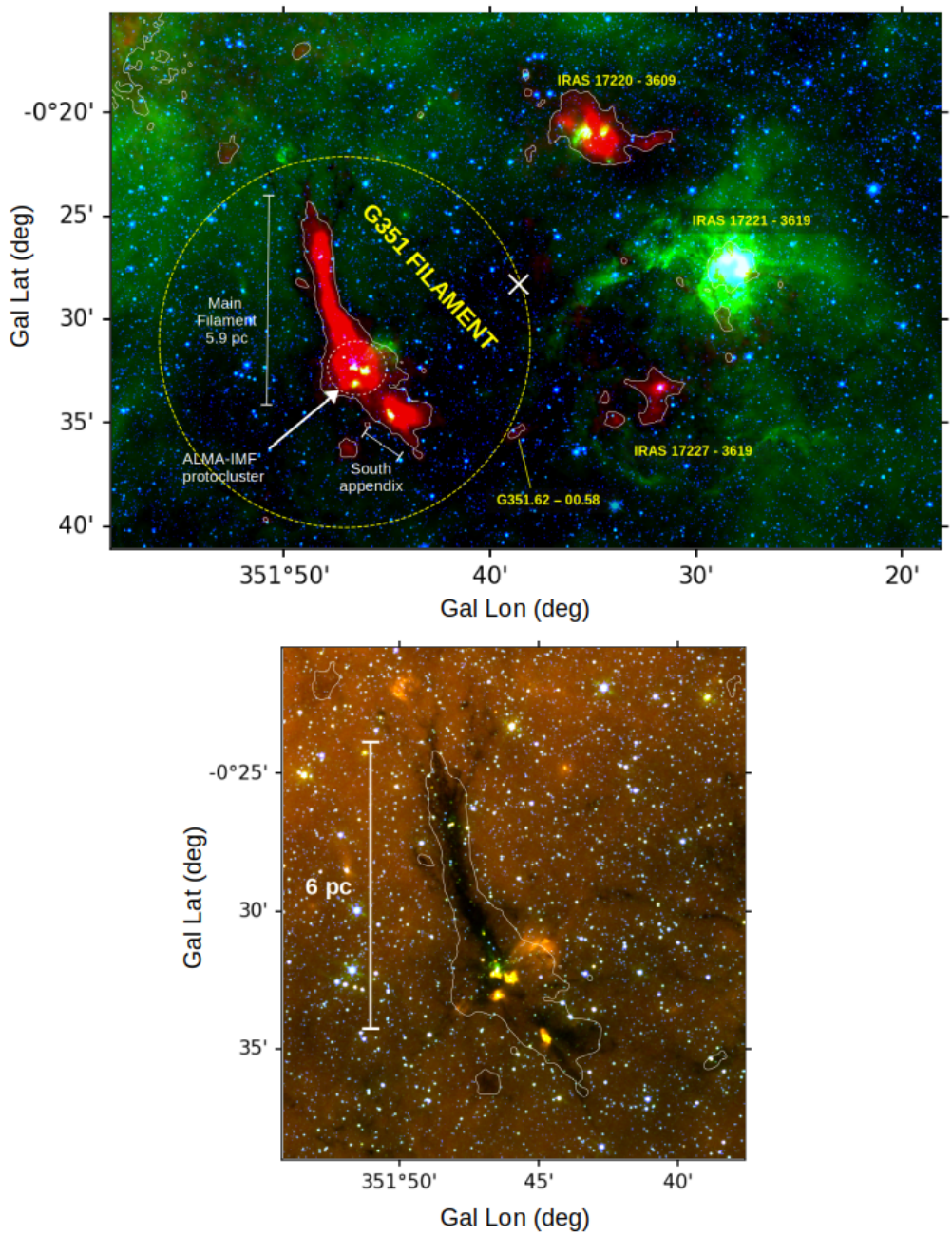

Figura 1.0.1: Top: Overview of the G351 Environment in a composite color map. The APEX+Planck dust emission at 870 μm is shown in red, the IRAC 8.0 μm in green, and the IRAC 3.6 μm in blue. An APEX+Planck contour level of 0.75 Jy/beam is drawn in white, and notice that it also covers the source IRAS 17221−3619, revealing that the dust emission is also bright in that area. The white x-symbol shows the center of our catalog searches for the G351 Environment, and the larger circle shows the area used to retrieve catalogs for the G351 Filament. Bottom: Zoom-in to the G351 Filament field in a color composite of three IRAC bands, where 8.0, 5.8 and 3.6 μm are shown in red, green and blue, respectively. The contour represents the same emission as in the top panel. This panel highlights, in an arbitrary color scale, that the cloud appears dark in the mid-infrared. The bright nebulous region locates the active protocluster, where cluster and massive star formation is ongoing.

filamentary body in which the protocluster is embedded and the curved structure of small clouds that follow the filament from south to west. All together form a non-continuous semi-circular path in the sky at 870 μm that plausibly belongs to the same molecular environment (but see below). We will call this entire field the "G351 Environment". Secondly, we define a small sub-field of the G351 Environment that is centered on the G351 protocluster. This includes the filamentary body in which the protocluster is embedded, together with the small vestigial appendix seen just below. This field will be called the "G351 Filament" hereafter and it is the structure that this work studies in detail. Given the intense interest in protocluster formation specifically, the ALMA Large Program ALMA-IMF (e.g. Motte et al., 2022; Ginsburg et al., 2022; Cunningham et al., 2023, Sandoval-Garrido et al., in prep.) focuses on the G351 protocluster itself (along with 14 other Milky Way protoclusters) at high resolution at 1 mm and 3 mm. Hence, the G351 filament itself can be subdivided into different components. These are the filamentary body stretching northward from and including the protocluster, which we will call the Main Filament (MF), and the small vestigial appendix seen immediately south of the protocluster, which we will call South Appendix (SA). See Fig. 1.0.1 for an overview of the G351 Environment and G351 Filament.

Line velocity measurements across the entire G351 Environment suggest that most of the bright emission at 870 μm are associated. Leurini et al. (2011b) spectra of ^{13}CO (2−1), C^{17}O (2−1) and C^{18}O (2−1) reveals that the two velocity components ~ -3 km s^{-1} and ~ -22 km s^{-1} are common for three bright sources in this path (SA, G351.62 and IRAS 17227−3619), while the velocity ~ -3 km s^{-1} is detected across all the MF and the velocity ~ -22 km s^{-1} is detected in IRAS 17221−3619. Furthermore, Ryabukhina and Zinchenko (2021) spectra of CO (2−1) completes this picture by detecting the same two velocities in one clump of the MF and the SA (clumps 6 and 5 in figure 5 of Ryabukhina and Zinchenko 2021).

Here, we undertake a systematic investigation of the G351 cloud and its sub-regions (see above) to compare both the gas mass reservoir and star formation properties with nearby

clouds, such as Orion A and California. We selected as our principal reference star forming site the Integral Shaped Filament (ISF) in the Orion A cloud for two reasons. It has a filamentary structure of similar length ($L_{ISF} = 7.3$ pc; Stutz and Gould 2016) as G351, and it is a well-studied high mass star forming site, both in terms of the global YSO content and the gas properties (e.g., Megeath et al., 2012, 2016; Stutz and Gould, 2016; Stutz, 2018; Sadavoy et al., 2016; Kainulainen et al., 2017; González Lobos and Stutz, 2019). Hence, the ISF is currently the prime candidate to establish comparisons regarding star and cluster formation in filaments. We also compare to the California L1482 cloud (Álvarez-Gutiérrez et al., 2021) because it has a similar mass to that of Orion A but lower star formation activity and hence might span a lower or early phase toward cluster formation (Lada et al., 2009).

This paper is organized as follows. We begin by determining the Gaia-based distance to G351 by applying techniques for identifying members in the Gaia DR3 catalog. We then determine the cloud gas properties using data from the ATLASGAL, Planck, and Herschel surveys. We focus on the gas line-mass *profile* of this filamentary cloud, which can be directly compared to that of the Orion A and California clouds. We then show that at our established distance, G351 exceeds the line mass of the ISF, the most active star forming region within 1 kpc of the Sun (Megeath et al., 2016). Finally, we show that the apparent star formation, averaged over the $\sim$2.5 Myr average lifetime of dusty YSOs, is deficient compared to the Orion A cloud, even with completeness corrections. We discuss observational biases that could result in this underestimate, and the implications for a difference in the intracloud SF-relation.

Capítulo 2

Data

Several archival data sets were used for this work, including point source catalogs built upon visible and infrared data, and imaging data in the infrared and sub-millimeter. We overview these data sets in this section.

2.1. Point source catalogs

Point sources were retrieved using cone searches as follows: the G351 Filament field was centered at the coordinate RA = 7 : 26 : 42,620, DEC = −36 : 09 : 22,473, with a radius of 0.15 degrees (dashed circle in Fig. 1.0.1), and the G351 Environment field was centered at the coordinate RA = 17 : 26 : 04,9607, DEC = −36 : 13 : 39,055 with a radius of 0.22 degrees (the ×-symbol in Fig. 1.0.1 shows the center of the search area).

We use the Gaia Data Release 3 (Gaia DR3) to leverage its accurate parallaxes (ϖ) and proper motions (μ). We also use the Glimpse catalog because it provides high sensitivity infrared photometry. Specifically, we use the Glimpse II Epoch 1 December '08 Archive version because it provides the largest number of sources over the G351 region.

2.1.1. YSO catalogs

We use the three public catalogs that have identified YSOs in the G351 Filament and Environment. They are i) the Kuhn et al. (2021b) catalog, which identified 75 YSOs in our G351 Filament field using a machine learning approach applied to the Spitzer/IRAC photometry combined with 2MASS and other ground-based near-IR photometry, ii) the Chen et al. (2013) catalog of extended green objects (EGOs), which identified 4 objects (all along the higher N(H_2) density filament) also using Spitzer imaging from the Glimpse survey, and iii) the Marton et al. (2019) catalog, which identified several YSOs in a probabilistic manner. In particular, the probabilistic nature of the latter motivates us to briefly describe its more relevant parameters as we will use them to filter its data. Marton et al. (2019) identified YSOs based on Gaia DR2 crossmatched with AllWISE. They first determined the probability for the 12 and 22 μm AllWISE bands to be real detections (P_R). Then, they defined two types of YSO probabilities: one based on all four WISE bands (PL_Y), provided $P_R > 0{,}5$; and the other based on the two shorter wavelength bands (PS_Y), provided $P_R \leq 0.5$.

2.1.2. YSO identification

In addition to these three catalogs, we independently identify YSOs following the phase-1 method (ph1) described in Gutermuth et al. (2009) and in Gutermuth et al. (2010). This method identifies YSOs using several criteria that use the four band 3.6-8 μm photometry. As a first step, it identifies contaminants such as galaxies with bright emission in the PAH features, knots of shock excited emission, PAH-contaminated apertures, or active galactic nuclei (AGNs). Then, from the remaining sources, it identifies Class I or Class II YSOs. We apply these criteria to sources with photometric uncertainties $\sigma < 0{,}2$ mag only. In the G351 Filament field we identify 61 YSOs, and after merging these YSOs to the existing YSO catalogs described above, we obtained 106 YSOs (used in Section 5). In parallel, for the G351 Environment the final merged

catalog has 225 YSO candidates (used in Section 3.2).

2.1.3. YSO catalog for Orion A

We use the Megeath et al. (2012, 2016) YSO catalog. It provides near- and mid- infrared photometry for Orion A and B sources, classifying them as e.g. protostars or disks. It is the most complete YSO catalog over this area and we particularly use their protostars classified as 'reliable' in Section 5.3.

2.2. Imaging

We use the APEX+Planck dust emission map that results from combining Planck/HFI and APEX/LABOCA data from the ATLASGAL survey (Csengeri et al. 2016). This data set is publicly available[1]. We also use Herschel images at 70, 160, 250, 350 and 500 μm from the Hi-GAL survey. Lastly, we use images at 3.6, 5.8, and 8 μm from the IRAC camera on board of the Spitzer telescope.

[1] https://atlasgal.mpifr-bonn.mpg.de/cgi-bin/ATLASGAL_DATABASE.cgi

Capítulo 3

Distance

The distance to the G351 protocluster is poorly constrained in the literature with differences of factor of $\sim$2 in the reported values (see above). We measure a distance based on the astrometry of Gaia DR3 assuming that a molecular cloud hosting several stars will exhibit clumping of sources in proper motion and parallax space. In this regard, we adopt two approaches: In method 1, we use the astrometry of the large Gaia DR3 catalog. In method 2, we use the astrometry of previously identified YSOs. On one hand, method 1 has the advantage of a larger sample size, but its drawback is that many foreground and background sources are included. On the other hand, method 2 has the advantage of relying on objects that are much more likely to belong to the cloud environment, but its drawback is the sample size. Despite these differences, the two methods retrieved similar results. The distance obtained from method 1 is 16 % larger than that obtained from method 2, and in the context of a large disagreement in the literature, this difference is small. We adopt the average between our two results (2.12 and 1.82 kpc, but see below), and report a constrained distance $D = 2 \pm 0{,}15$ kpc for the G351 protocluster and its filament.

We selected a strict threshold of $0.5''$ for all the catalog-crossmatches we performed in this work. In addition, for each crossmatch we performed a correction consisting in

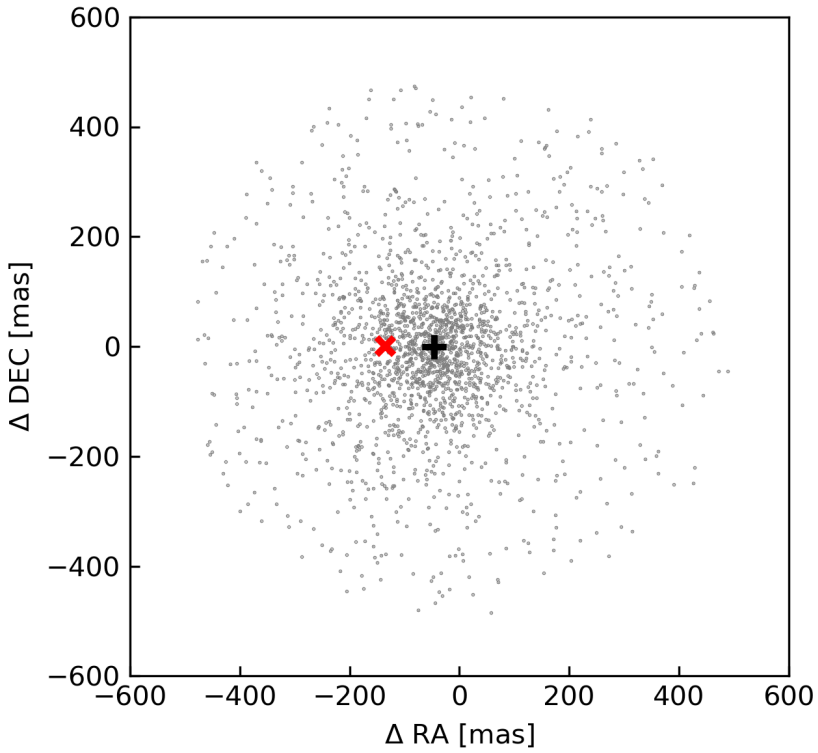

Figura 3.0.1: Example of our 2-step crossmatch process for Gaia DR3 and Glimpse in the area of the G351 Filament. We show the separations of the matched sources after correcting the relative positional shift $\langle\Delta\text{RA}\rangle$ and $\langle\Delta\text{DEC}\rangle$ between the two catalogs. The red $\times$-symbol represents the original positional shift $\langle\Delta\text{RA}\rangle = -135$ mas ; $\langle\Delta\text{DEC}\rangle = 1{,}04$ mas, and the black plus-symbol shows the subsequently reduced shift $\langle\Delta\text{RA}\rangle = -45$ mas; $\langle\Delta\text{DEC}\rangle = -1{,}23$ mas.

two steps. First, by running the crossmatch the first time we obtained the systematic positional shift between the catalogs, which is represented by the average separation of the matching sources for each coordinate, i.e. $\langle\Delta\text{RA}\rangle$ and $\langle\Delta\text{DEC}\rangle$. Then, we subtracted these quantities to one of the catalogs and reran the crossmatch. As a result, the updated positional shift gets reduced (sometimes significantly) and in some cases the number of matched sources increased. This way our crossmatches account for positional shifts that are sometimes present between some catalogs.

Figure 3.0.1 shows this process for the Gaia DR3 and Glimpse samples over the G351 Filament field (see Method 1 below). Both catalogs have a systematic positional shift relative to each other, and that average shift is shown by the red x-symbol. At this

point before correction, the number of matched sources was 1975. After correction, even new pairs of matches were found, reaching a total of 2024 matches. The updated average shift has a significant reduction as shown by the plus-symbol, and we note that here it does not reach the origin exactly because of the new matches we found. We also corrected all parallaxes in our data from a systematic bias following the recipe of Lindegren et al. (2021). They found that this bias produces an offset of a few tens of milliarcseconds, for which the main dependencies are the magnitude, colour, and ecliptic latitude. The newly corrected parallaxes are ϖ' hereafter. Their tentative recipe for correction is publicly available[1].

A caveat to consider on both distance methods is a possible selection effect due to the Gaia limitations to detect the most redder sources, which might bias our results towards a closer distance. YSOs are inherently red and, combined with the high reddening throughout the cloud, they should give an optical telescope like Gaia preferential access to the closest and less embedded objects. We note, however, that our strict catalog crossmatches provide the certainty that the astrometry we are using actually correspond to the infrared detected sources we use in method 2 (and also in our alternative approach in method 1).

3.1. Distance method 1

We use the Gaia DR3 sources over the G351 Filament field, which contains 3831 point-sources (see Fig. 1.0.1 for an overview of the field and Section 2 for the parameters of the searched area). We sliced this large Gaia DR3 sample in ϖ' ranges of 0.05 mas to analyze individually their distribution in proper motion space and search for any possible clustering. Here, we distinguish those sources with low proper motion error $\sigma_\mu < 0{,}3$ mas yr^{-1} from those with larger σ_μ. By visually inspecting each parallax slice, we observe only one of them exhibiting a clustering dominated by low σ_μ sources

[1]The *zero_point* python package. Example code in ESA website: https://www.cosmos.esa.int/web/gaia/edr3-code

(Fig. 3.1.1, top panel). This particular slice $\varpi' \in$ [0.45,0.50] mas contains 137 sources, and we identify its overdensity as all the sources enclosed by a circle centered at $\mu_{RA}* = -1.35$ mas yr^{-1} and $\mu_{DEC} = -2{,}9$ mas yr^{-1}, with radius 1.05 mas yr^{-1}. This circle is shown in black in Fig. 3.1.1 and it encloses 27 sources. From this overdensity we estimated an error-weighted mean parallax of $\langle\varpi'\rangle = 0{,}471 \pm 0{,}020$ mas, equivalent to a distance $D = 2{,}12 \pm 0{,}09$ kpc.

The bottom panel of Fig. 3.1.1 shows the positions of the circled sources of the top panel with a black ring over each. Despite sharing very similar proper motions, they do not appear spatially clustered or tightened to the filament. It should not be expected, however, that these sources appear highly clumped in position as they do in proper motion, because the cloud is dark for telescopes in the optical/IR, as shown by Fig. 1.0.1 (right panel), and a degree of spatial dispersion around the cloud would result from a somewhat more evolved population of stars associated with the G351 filament. Finally, we note as well that if adopting a less strict proper motion error $\sigma_\mu < 0{,}4$ mas yr^{-1}, then a second clump dominated by low σ_μ appears in proper motion space but for a larger parallax range. However, we report a distance based on the data slice of Fig. 3.1.1 because its clump has lower σ_μ and its resulting distance is relatively close to that of method 2.

In an alternative approach of this method we introduced Spitzer point sources by crossmatching our Gaia DR3 sample with Glimpse. This intends to filter out from the Gaia DR3 sample those objects that are bright in the visual but faint in the infrared, and therefore − conveniently − raising the proportion of reddened sources. In that case, we would again observe that the same slice $\varpi' \in$ [0.45,0.50] mas is the only one exhibiting a clump dominated by low $\sigma_\mu < 0{,}3$ mas yr^{-1} sources, and the error-weighted mean parallax would be $\langle\varpi'\rangle = 0{,}470 \pm 0{,}021$ mas, calculated from 24 circled sources (instead of 27) and equivalent to a distance $D = 2{,}13^{+0{,}10}_{-0{,}09}$ kpc. This alternative procedure for method 2 introduces one extra step that barely modifies the distance estimation, but we believe it is reasonable to discuss.

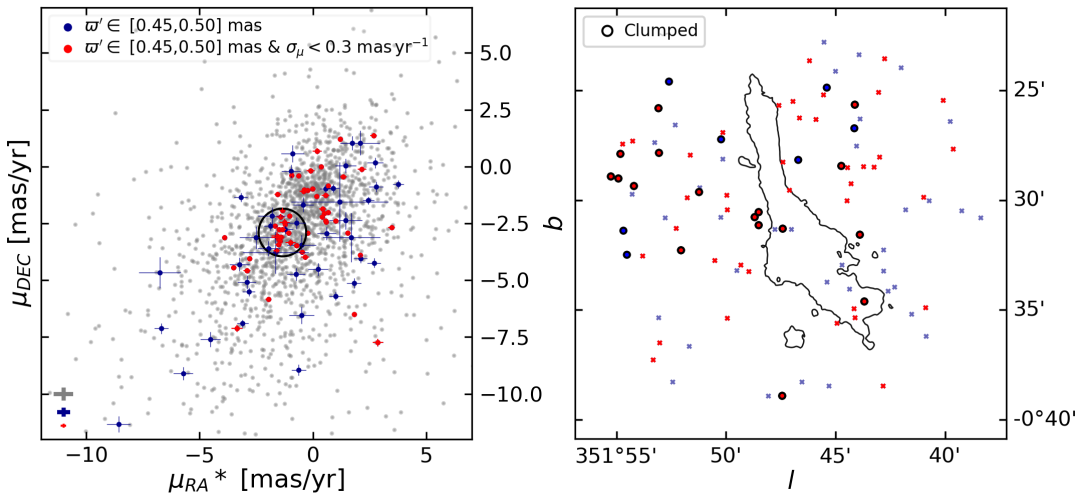

Figura 3.1.1: Gaia DR3 sources with parallax ϖ' between 0.45 and 0.50 mas (red and blue dots). The red dots have low proper motion error $\sigma_\mu < 0{,}3$ mas yr^{-1}. Left: The circle highlights the sources that appear to be clumped in proper motion space, while the background grey dots show a *zoomed-in* section of the whole Gaia DR3 proper motion distribution. The bottom left error bars show the mean proper motion error of the three data sets in their respective colors, and we note that the error bars of the low error sources in red are smaller than the marker size. Right: Galactic positions of the Gaia sources. We mark the 27 sources inside the black circle of the left panel with a black ring, and we mark those outside as x-symbols to make the contrast easier. The G351 filamentary structure is represented as an APEX+Planck contour level of 0.75 Jy/beam as in Fig. 1.0.1.

3.2. Distance method 2

Here we consider only YSOs with IR excesses from dusty disks or envelopes to increase the certainty that the sources under study are associated with the cloud, following the strategy of Kuhn et al. (2021a). Their approach has proven to work efficiently in Galactic clusters with parallax reaching $\varpi \sim 0{,}5$ mas on average (Kuhn 2022, private communication). As the number of YSOs is small over the G351 Filament field, we expanded our search field to include the few clouds that are plausibly associated to the same molecular environment as that of the filament (i.e. the G351 Environment field).

This larger-field YSO sample has 225 YSOs (Sections 2.1.1 and 2.1.2), but it gets significantly reduced to 29 sources when crossmatched with Gaia DR3. Furthermore, we selected only those YSOs with proper motion error $\sigma_\mu \leq 0.4$ mas yr^{-1}. We also kept

only those Marton et al. (2019) YSOs whose probability to be actual YSO was larger than 0.8. This means that $PL_Y \geq$ 0,8 when $P_R > 0.5$, and $PS_Y \geq 0{,}8$ when $P_R \leq 0.5$ (Section 2.1.1). We applied these cuts on the data to avoid including high uncertainty measurements, while preserving a significant number of sources. The final sample has 16 YSOs detected by Gaia within the G351 Environment.

Fig. 3.2.1 shows a concentration of YSOs in parallax for both ϖ' versus μ spaces (top panels). It appears particularly clear in the parallax versus μ_{RA} panel as a compact clump of sources (top left). We selected as clump members those sources in the range $\varpi' \in$ [0.28,0.7] mas (shaded area in Fig. 3.2.1) because they are visually associated and because of their error bars. This leaves us with 10 clump members for the average parallax calculation, while the other 6 are considered contaminants. The error-weighted mean parallax of this clump is $\langle \varpi' \rangle = 0.55 \pm 0{,}015$ mas, which corresponds to a distance $D = 1.82 \pm 0{,}05$ kpc.

Our procedure is different than that adopted by Kuhn et al. (2021a), but it is driven by the smaller number of YSOs in our sample, together with the clear presence of (low-uncertainty) outliers and near zero parallaxes that can heavily influence the average result. We also note that if adopting a P_R limit different than 0.8 for the Marton et al. (2019) catalog sources, the resulting distance might decrease to 1.74 kpc (for $P_R > 0{,}6$), but for the rest of the P_R limits we tested (down to $P_R \geq 0{,}5$), the resulting distance varies within the range 1.79 and 1.84 kpc. We attribute this variable result to a sample selection effect driven mostly by the limited number of sources we have, but we consider as well that all these distances we get are similar, so that we can rely on the more conservative criteria $P_R > 0.8$.

Another caveat is that three out of the ten clump member YSOs lie over the area of the source IRAS 17220-3609 (see point sources in Fig. 3.2.1, bottom right panel. Also see Fig. 1.0.1), which is unlikely to belong to the G351 molecular environment given its very different molecular line velocity (Leurini et al., 2011b). However, we still included

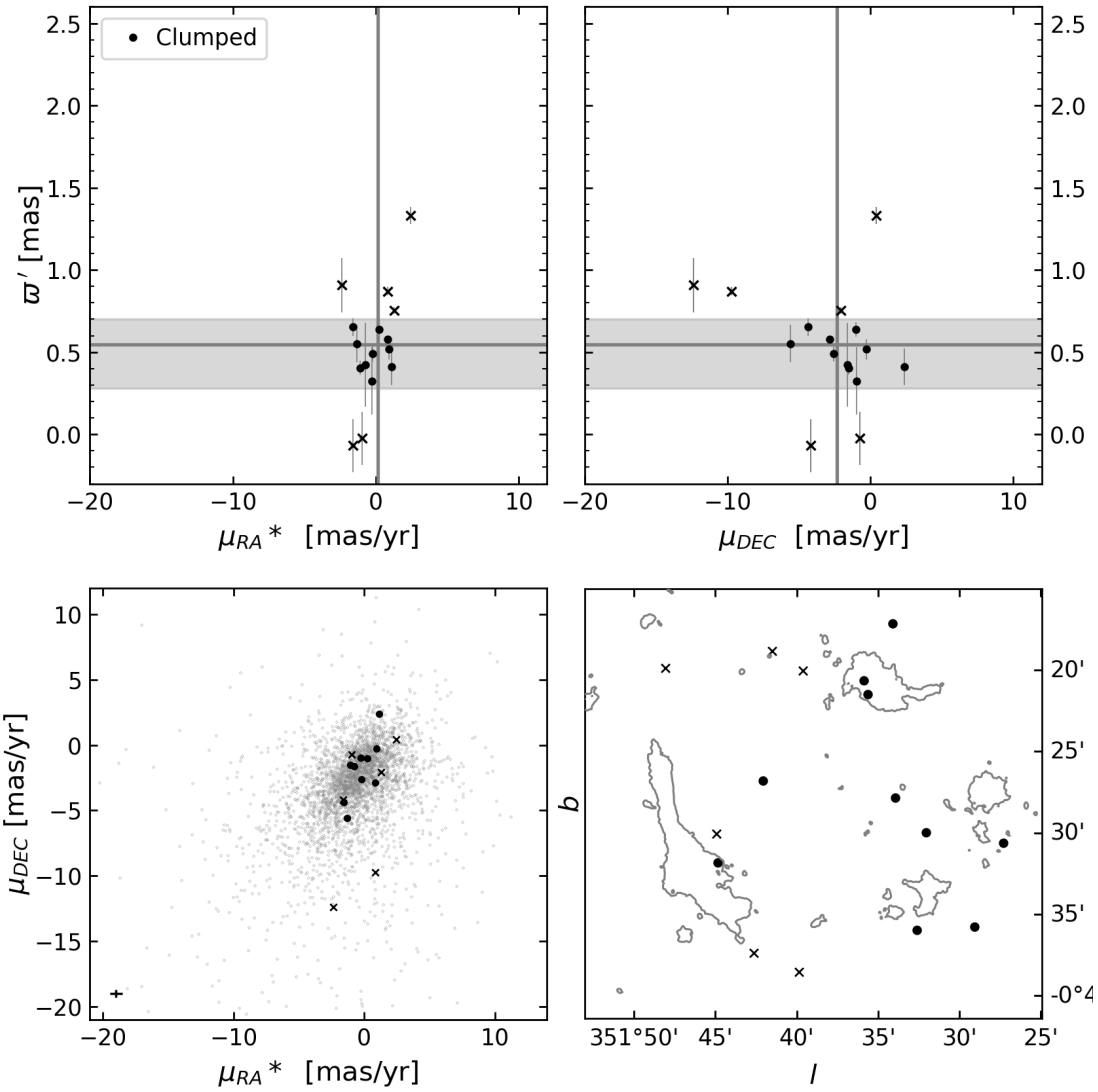

Figura 3.2.1: Astrometry of the 16 Gaia DR3 detected YSOs with a low proper motion error $\sigma_\mu \leq 0{,}4$ mas yr^{-1} in the G351 Environment field. Top panels: corrected parallaxes versus Right Ascension (left) and Declination (right) proper motions. The shaded area highlights the space where the sources clump, and those inside that area are shown as solid dots while those outside are shown as x-symbols (same symbology for bottom panels). The horizontal and vertical lines crossing both frames show the mean ϖ' and mean μ, respectively, of the clumped sources (i.e. the solid dots). The grey bars are the 1-σ uncertainties for ϖ'. Bottom left: proper motions against the whole Gaia DR3 raw catalog (grey background). The small bar at the bottom show the mean σ_μ of the 16 low-error YSOs. Bottom right: galactic positions of the 16 YSOs. Contours represent an APEX+Planck emission level of 0.75 Jy/beam as in Fig. 1.0.1.

them because there is no certainty about what environment they belong to. Although it is difficult to be certain about what is the correct molecular environment of G351, we highlight that our sources still clump in parallax, which agrees with a system that is physically associated.

Capítulo 4

Mass and Line-mass

4.0.1. Column density map

We retrieved a total of six multi-wavelength image data (70, 160, 250, 350, 500, and 870 μm) to reconstruct the black-body spectral energy distribution (SED) and then produce the column density N(H_2) map of the G351 filament. The far-IR data from 70 μm to 500 μm are from the Hi-GAL survey. The 870 μm data are from the APEX telescope large area survey of the galaxy (ATLASGAL, Csengeri et al., 2016), which are combined with Planck data to recover the missing flux in the data processing.

The data products are firstly converted into the uniform unit of "MJy/sr" based on the nominal beams of original images. Then we convolved the images to the same angular resolution of $45''$, with a Gaussian kernel of $\sqrt{(45'')^2 - \theta_\lambda^2}$ where θ_λ is the HPBW size of the point spread function of the radio beam. Then the convolved data from the different bands were regridded to a common pixel size of $11''$,5.

We have used the smoothed far-IR to sub-mm image data to obtain intensity as a function of wavelength for each pixel, which we model as a modified blackbody:

$$I_\nu = B_\nu(T_{\rm dust})\left(1 - e^{-\tau_\nu}\right), \tag{4.0.1}$$

where the Planck function $B_\nu(T_{\rm dust})$ is modified by optical depth,

$$\tau_\nu = \mu_{\rm H_2} m_{\rm H} \kappa_\nu N({\rm H_2}) / R_{\rm gd}. \tag{4.0.2}$$

Here $\mu_{\rm H_2} = 2{,}8$ is the mean molecular weight adopted from Kauffmann et al. (2008), m_H is the mass of a hydrogen atom, $N({\rm H_2})$ is the column density of hydrogen molecule (H_2), and $R_{\rm gd} = 100$ is the gas-to-dust ratio. The opacity κ_ν can be expressed as a power-law in frequency as,

$$\kappa_\nu = 3{,}33 \left(\frac{\nu}{600\,{\rm GHz}}\right)^\beta \,{\rm cm^2\,g^{-1}}, \tag{4.0.3}$$

where $\kappa_\nu(600\,{\rm GHz}) = 3{,}33\,{\rm cm^2\,g^{-1}}$ is the dust opacity for coagulated with thin ice mantles (retrieved from column 5 of Table 1 in Ossenkopf and Henning 1994). The dust emissivity index has been fixed to be $\beta = 2{,}0$, in agreement with the standard value for cold dust emission (Hildebrand, 1983). The free parameters in the model are the dust temperature and column density. The pixelwise fitting was performed using the `least-square` method, only when the pixels have positive intensities in all the five far-IR images.

4.0.2. Background subtraction and cumulative mass

We use the N(H_2) map to estimate the total mass of the filament and derive related metrics, such as the cumulative mass profile, the line-mass profile and the SFE. In the following we describe how these parameters are obtained.

First of all, we subtracted a uniform background contribution to the N(H_2) map. The subtracted level corresponds to the peak in the pixel noise distribution, which leads to a 13 % reduction of the total emission. After that, we converted N(H_2) into mass M using the equation given by

$$M = m_H\, \mu_{H_2}\, N({\rm H_2})\, A_{\rm pix} \tag{4.0.4}$$

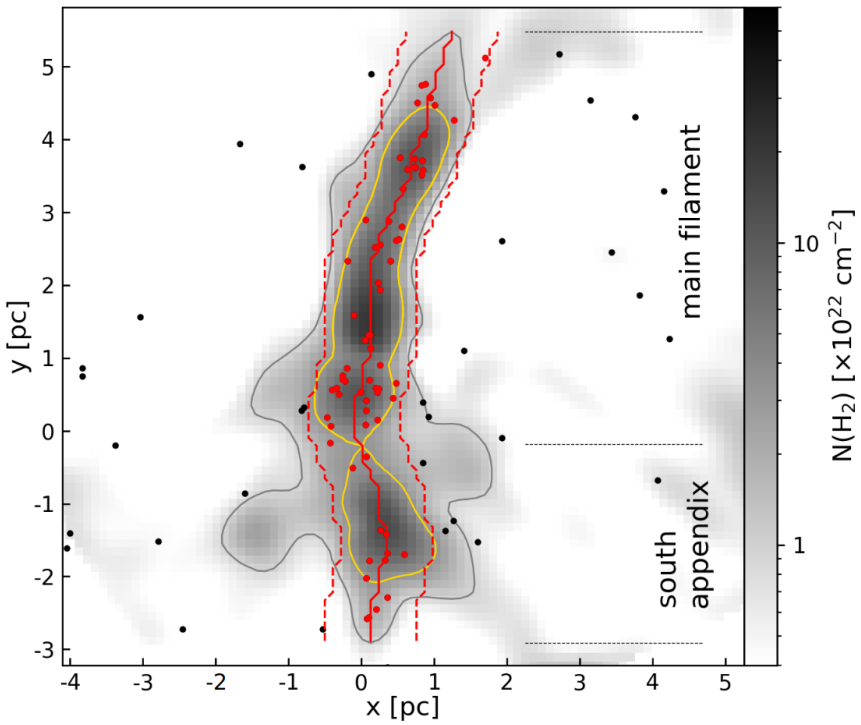

Figura 4.0.1: Rotated (see text) Herschel N(H_2) map of the G351 Filament. We outline the two main components of the filament (MF and SA), together with the distribution of all the 106 IR- detected YSOs. The red solid curve show the filament's ridgeline, and the two red dashed curves are 0.63 pc offset copies of the ridgeline, representing the maximum width of the cloud (Section 4.0.3). The 68 YSOs enclosed within this projected width from the ridgeline are shown with red symbols, while those outside that width are shown in black. A contour level of 9.2 $\times 10^{21}$ cm^{-2} (in grey) was used to define the maximum length of the filament, and the contour level 3.2$\times 10^{22}$ cm^{-2} was used to define the interface between the SA and MF.

where $A_{\rm pix}$ is the area of a pixel. This derived mass map is the starting point of this analysis.

In order to derive any mass metrics, we first rotated the map such that the longitudinal dimension of the filament is aligned as much as possible with the map pixel columns direction as shown in Fig. 4.0.1. After that, we identified the ridgeline, traced by the maximum N(H_2) values at each slice in the y distribution of Fig. 4.0.1. Lastly, we determined the length of the filament from a contour criteria. We used the level 9.2 $\times 10^{21}$ cm^{-2} (grey contour in Fig. 4.0.1) because it encloses the cloud, capturing all its features, and the pixels at both ends define the G351 filament's length as $L_{G351} =$ 8,6 pc.

The next step was analyzing the longitudinal mass variations of the filament. Based on the smoothed ridgeline we re-arranged each map row horizontally to align the ridgeline pixels into the same column. Then, we calculated the cumulative mass with the varying y coordinate, summing up the mass from south to north for different widths w as shown in Fig. 4.0.2. This figure shows that the mass is distributed non-uniformly along the filament. We observe some jumps or curvatures due to higher mass concentrations at $\Delta y = 2$, 3.5, 5 and 7 pc approximately, and this occurs similarly for all widths we tested. Interestingly, the location of the protocluster at $\Delta y = 3.5$ pc is not the main jump, meaning that other portions of the filament are more concentrated. With this mass-declination dependency in mind, we proceed to compute the radially-projected gas line-mass profile of the cloud.

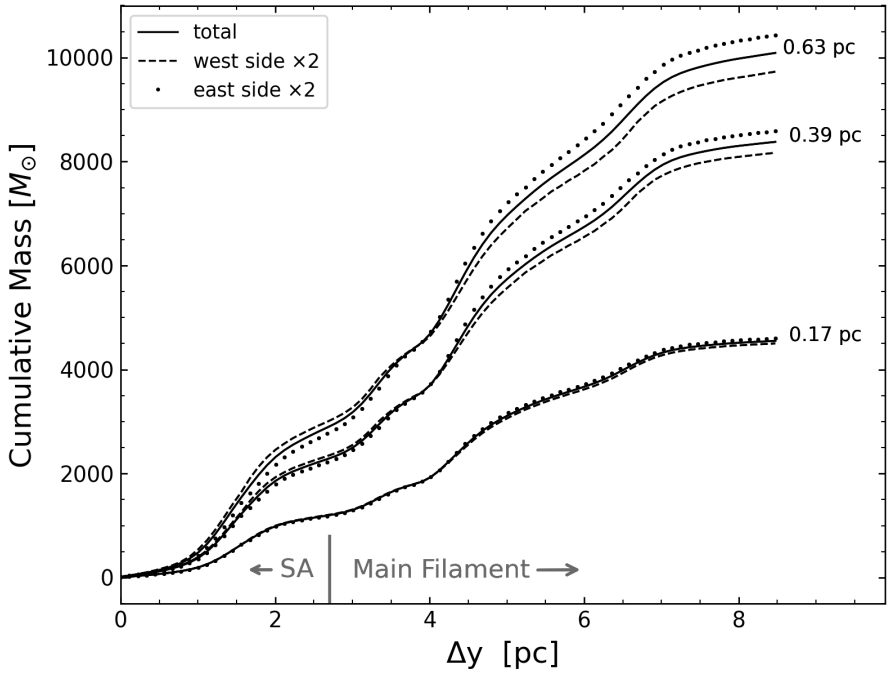

Figura 4.0.2: Enclosed cumulative mass along the G351 filament given a width w =[0.17, 0.39, 0.63] pc, counting from south to north. These three selected widths extend within the radial domain of the filament ($w \leq$ 0,63 pc), and their respective curves show similar variations, meaning that there is no significant dependency of the enclosed mass on the chosen width.

4.0.3. Line-mass profile, gravitational potential, and gravitational field

Following Stutz and Gould (2016) and Stutz (2018), the line-mass profile is the longitudinally-averaged gas distribution along a filamentary structure. Here, the cumulative mass M corresponds to the total enclosed gas mass at a given projected radius from the ridgeline. This enclosed mass is then divided by that (constant) length L. Formulated this way, this allows for fair comparisons between filamentary clouds of different masses and lengths.

The profile of G351 shown in Fig. 4.0.3 (black curve) is composed of two approximately straight components (in log−log space), which can be approximated with a power-law following

$$\lambda_{\rm app}(w) = \zeta \left(\frac{w}{\rm pc}\right)^{\gamma}, \tag{4.0.5}$$

where $\lambda_{\rm app}$ is the plane-of-the-sky (POS) projected line-mass, w is the projected radius from the ridgeline, and ζ is the 1 pc normalization in units of $M_\odot$/pc (see Table 4.0.1). Here, the inner curve at $r \lesssim 0.63$ pc is steeper with slope $\gamma = 0{,}62$, while the outer curve is flatter with slope $\gamma = 0{,}18$. We considered that the break at $w \simeq 0.63$ pc separating both components (vertical grey line in Fig. 4.0.3) represents the interface at which the sky emission dominates over the measured enclosed mass. For this reason, we adopted conservatively $w = 0.63$ pc as the total radial extent (from the ridgeline) of the cloud and hence report the fitting parameters of the inner component as representing the filamentary cloud entirely (Table 4.0.1). Our adopted total radial extent of the cloud ($2 \times w$) and its length $L_{G351} = 8{,}6$ pc enclose an area $A_{G351} = 11$ pc^2.

Given the longitudinal mass variations of the G351 filament shown in Fig. 4.0.2, we also estimate the individual profiles of the two main bodies that make up the whole G351 filament structure, i.e. the MF and the SA. We used the $N(H_2)$ contour level 3.2×10^{22} cm^{-2} (yellow contour in Fig. 4.0.1) to set the interface between the MF and the SA. Both profiles are slightly different to that of the total G351 filament: The MF

profile is 3.5 % higher while the SA profile is 7.5 % lower (see cyan and blue profiles respectively in Fig. 4.0.3).

Fig. 4.0.3 compares the G351 filament to some well-studied star forming regions in the Galaxy. Strikingly, G351 surpasses the line-mass profiles of most structures observed in Orion A and California. It is $\sim 3\times$ larger than that of the ISF, and also larger than that of the ONC at w $\geq$ 0,19 pc. Such a high line-mass profile confirms that the G351 filament contains a concentrated reservoir of dense gas available to fuel star formation now.

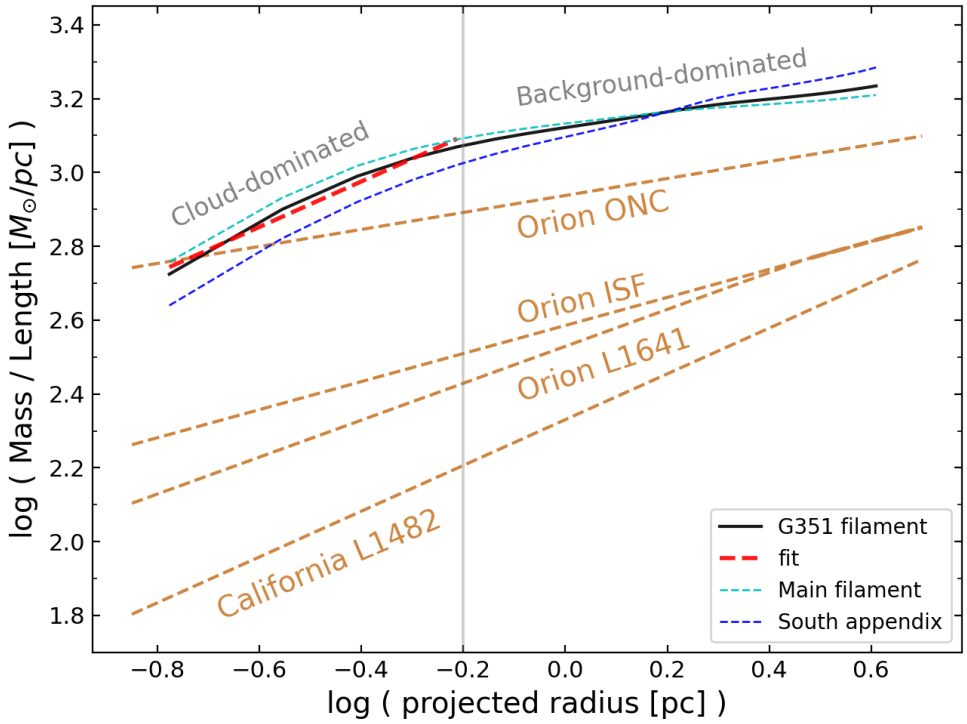

Figura 4.0.3: Enclosed gas-mass to filament-length versus projected radius from the N(H_2) ridgeline (black curve for G351). The red line is the linear fit we performed for the inner (cloud dominated) component. The profiles for both the MF and SA that make up the whole G351 filament body are included. The additional profiles of four relevant star forming regions (orange dashed lines) show that the G351 line-mass is comparatively large (Orion and L1482 profiles from Stutz and Gould 2016, Stutz 2018 and Álvarez-Gutiérrez et al. 2021).

Line-mass *profiles* (or M/L profiles) are fundamental for physically characterizing molecular clouds and their constituent filaments (Stutz and Gould, 2016; Stutz, 2018; Stutz et al., 2018; Álvarez-Gutiérrez et al., 2021, e.g.). Here, the ONC and G351 show that the two filaments have approximately similar M/L values at a specific radius, but have different profile shapes in M/L if the mass distribution is scrutinized as a function of distance from the filaments ridgeline. This information is lost when reporting a single M/L value. Overall, the above line-mass procedure has two small caveats. When projecting the original curvature of the filament towards the ridgeline, we are slightly reducing its length. Additionally, we assumed no inclination of the filament relative to the POS. These two caveats mean that our reported profile might be overestimating the actual profile of the filament, but the effect should be small. For instance, for an hypothetical inclination of 45° relative to the POS, the filament's length is larger by a factor of $1/\sqrt{2}$, and then the line-mass profile is reduced about a 30 %. Still, this is low compared to the e.g. 300 % difference relative to the ISF.

Given that the filament is highly symmetric about the ridgeline, and following Stutz and Gould (2016) and Álvarez-Gutiérrez et al. (2021), we derive from equation 4.0.5 various profiles that are consistent with this line-mass profile and which assume cylindrical geometry. Hence, the implied volume density $\rho_{\rm app}(r)$, gravitational potential $\Phi_{\rm app}(r)$, and the gravitational field $g_{\rm app}(r)$ profiles, respectively, are:

$$\begin{aligned}\rho_{\rm app}(r) =& \frac{\gamma(-\gamma/2)!}{2(-\gamma/2-1/2)!(-1/2)!}\frac{\zeta}{\rm pc^2}\left(\frac{r}{\rm pc}\right)^{\gamma-2}\\ =& \beta\left(\frac{r}{\rm pc}\right)^{\gamma-2};\end{aligned} \tag{4.0.6}$$

$$\Phi_{\rm app}(r) = \psi\left(\frac{r}{\rm pc}\right)^{\gamma}; \tag{4.0.7}$$

and

$$g_{\rm app}(r) = -\xi\left(\frac{r}{\rm pc}\right)^{\gamma-1}. \tag{4.0.8}$$

We list in Table 4.0.1 the values for β, ψ, and ξ. As shown in Álvarez-Gutiérrez et al. (2021); Stutz and Gould (2016); Stutz (2018); Stutz et al. (2018), these profiles can be compared to other observables, such as the gas velocities in the presence of e.g., rotation and oscillations, to physically characterize the filament-averaged properties.

Region	ζ^a $M_\odot pc^{-1}$	β^b $M_\odot pc^{-3}$	ψ^c $(km\ s^{-1})^2$	ξ^d $(km\ s^{-1})^2 pc^{-1}$	γ^e	Proj. length pc	Gas mass $M_\odot$
G351	1585	75.1	10.56	6.55	0.62	8.6	10200
G351 M. Filament	-	-	-	-	-	5.9	6900
G351 S. Appendix	-	-	-	-	-	2.7	2700
Orion ISF [1]	385	16.5	6.3	2.40	0.38	7.3	6200
Orion L1641 [1]	338	16.1	3.50	1.80	0.50	23.2	2×10^4
Orion ONC [2]	866	25.9	27.60	6.40	0.23	0.5	1300
California L1482 [3]	214	10.2	1.45	0.89	0.62	9.4	4260

Cuadro 4.0.1: Line-mass and star forming metrics. Remarks: [a]for equation 4.0.5, [b]for equation 4.0.6, [c]for equation 4.0.7, [d]for equation 4.0.8, [e]power-law index from fitting the line-mass profile in Fig. 4.0.5. Comparison regions: [1,] Stutz and Gould (2016); [2]Stutz (2018); [3]Álvarez-Gutiérrez et al. (2021)

4.0.4. Total gas mass of the cloud

With the radial extent of the cloud constrained to the inner component of the profile, we report a total gas mass $M_{gas} = \sim$10 200 $M_\odot$ ($w \leq 0.63$ pc) for the G351 filament as a whole (see Fig. 4.0.2). This mass metric is about 4× larger than the ∼2300 $M_\odot$ ($w \leq 0.63$ pc) of the ISF (Stutz and Gould 2016, see their figure 4), and larger than those of the other regions we are comparing G351 with, except L1641 which is a much larger scale structure but with a much lower line mass profile. The POS-projected lengths of each structure of Fig. 4.0.3 and their respective gas masses are also listed in Table 4.0.1. We compare our result to the literature, scaling to our assumed distance when necessary. Our gas mass agrees to within 4 % with the Leurini et al. (2019), when we integrate within the same $N(H_2)$ level. On the other hand, Ryabukhina and Zinchenko (2021) reports a mass of 1800 $M_\odot$ (7200 $M_\odot$ scaled to our distance) using $C^{18}O$ (2-1) molecular data, so within ∼ 30 % of our measurement. However, as they discuss, some negative flux features in their $C^{18}O$ (2-1) spectra might cause some underestimate. We

conclude that the agreement, despite the very different techniques, is excellent.

Overall, these results firmly establish that G351 is both more massive and compact towards its ridgeline than the ISF, and the reader may − reasonably − wonder at this point if the G351 star forming activity at least resembles that of the ISF (see Fig. 4.0.3).

Capítulo 5

Discussion

We examine the G351 star forming activity by leveraging our catalog of YSOs and gas mass map. We start by comparing the number of YSOs per (longitudinal) parsec that G351 and the Orion A filaments are forming, taking into account incompleteness effects due to their $\sim 5\times$ different distances and the different sensitivities of the Spitzer Survey of Orion and the Glimpse Survey. Accounting for this incompleteness will enable us to estimate the G351 SFRs and SFEs, and will provide the means to compare the SFR and SFE per free-fall time as a function of cloud density to those values in nearby clouds.

5.1. YSO incompleteness

The Spitzer Orion survey has provided a relatively complete survey of dusty YSOs in the Orion molecular clouds down to the hydrogen burning limit for a 1 Myr population, except in regions of bright nebulosity (Megeath et al., 2016). As G351 is five times more distant than the Orion A clouds ($D_{Orion\,A} \sim 390$ pc for the ISF; Kounkel et al. 2017; Stutz et al. 2018), we must address the effect of incompleteness on the YSO counts measured in G351. Outside of the protocluster, the dark, high extinction regions of the cloud show a low density of sources and are devoid of bright nebulosity (see Fig. 1.0.1, right panel). Accordingly, we do not expect source confusion to have a

significant influence on the estimated YSO numbers. We therefore focus our analysis on how the lower photometric sensitivity of the Glimpse survey combined with the larger distance to G351 reduce the number of detected YSOs. We do this by using the Spitzer survey of the Orion A cloud as a benchmark, calculating the number of Orion YSOs that would be visible at the 2 kpc distance of G351 if observed with the sensitivities of the Glimpse survey.

For this, we use the Spitzer point-source catalog of Megeath et al. (2012) and the YSOs identified from that catalog published by Megeath et al. (2012) and Megeath et al. (2016). For each source in the Spitzer point source catalog, we shifted the magnitude by the difference in the distance modulus of the two clouds: 1.75 mag. We then use data from the Glimpse survey (Benjamin et al., 2003; Churchwell et al., 2009) to find the median uncertainty at that magnitude; due to the lower integration time of the Glimpse survey these uncertainties are higher than those in the Spitzer Orion Survey. Using this relationship between magnitude and uncertainty for all four Spitzer bands, we assigned each source in the shifted Spitzer Orion catalog the uncertainty it would have if it were in the Glimpse survey. We then rerun the YSO identification criteria from Megeath et al. (2012) and Megeath et al. (2016) on the IRAC data alone, ignoring criteria that use the 2MASS magnitudes or the 24 μm data. The criteria employed at this point are the same as the Gutermuth et al. (2009) criteria (ph1) that we use here for Glimpse data (see Sec. 2.1.2).

This process provides a catalog of YSOs that would be detected by Glimpse at 2 kpc, and we notice that it keeps a fifth of the sources of the original catalog for Orion A. We consequently apply this correction factor $k = 5$ to compare line densities and to give context to the G351 SFE and SFR.

	Total N_{YSO}	Enclosed N_{YSO}	Enclosed N_{YSO}/L
G351	61	39	4.5
Orion A ISF	195	161	22
Orion A L1641	114	54	2.3

Cuadro 5.1.1: Number of detected YSOs in G351 compared to the completeness corrected numbers of YSOs that would be detected in Orion A assuming a distance D= 2 kpc. The enclosed N_{YSO} (third and fourth columns) are those within $w \leq$ 0,63 pc from the ridgeline of each structure, and N_{YSO}/L represents the corresponding N_{YSO} pc^{-1}. For G351, we used the phase-1 method for identifying YSOs, while for the Orion A structures we used an equivalent method described in Megeath et al. (2012) and Megeath et al. (2016) (see text). The lengths of each filament are listed in Table 4.0.1.

5.2. Line density of YSOs

We define the YSO line-density of a filamentary cloud as the longitudinally-averaged number of YSOs (N_{YSO}) that the cloud hosts per parsec, i.e. we divide N_{YSO} by the length L of the filament. Comparing G351 to the Orion A sub-structures (ISF and L1641) through this simple metric is a revealing exercise, and it needs 3 considerations: (1) The three clouds are elongated structures that can be modeled as filaments; (2) their lengths are different; and (3) the YSO incompleteness discussed above. To compare line densities as fairly as possible we selected for all the clouds (G351, ISF and L1641) those YSOs within a width $w \leq$ 0,63 pc from the respective ridgelines of those clouds. In addition, we considered only those YSOs that are identified by methods that use equivalent criteria. For G351 we use the phase-1 YSOs (Section 2.1.2), while for Orion A we use the YSOs that are detectable by Glimpse at 2 kpc as described in the above Section 5.1. We find that G351 hosts a factor of $\sim 5\times$ fewer YSOs per parsec than the ISF, after appliying the factor of $5\times$ completeness correction (see Table 5.1.1), revealing a lower star forming activity. Due to the possibility of incompleteness due to confusion in nebulous regions of the protocluster, we also calculate the value for the G351 filament north of the protocluster (MF-north; 19 ph1-YSOs, L= 4,5 pc) which is 4.2 YSOs pc^{-1}. We also note that in the G351 filament the average YSO separation from the ridgeline is 0.177 pc. These low values for G351 suggest tension with the

established SF-relations: the G351 gas is (4×) more massive and (3×) more compact towards its ridgeline than the ISF gas (Sections 4.0.3 and 4.0.4), but it is forming about 5× fewer YSOs per pc. We discuss plausible reasons for this below.

5.3. SFE and SFR

We measure the SFE and SFR from the YSOs at $w < 0{,}63$ pc from the G351 ridgeline. They are $N_{YSO} = 68$ from all the four catalogs described in Sections 2.1.1 and 2.1.2, out of the total of 106 YSOs over the G351 Filament field (see Fig. 4.0.1).

The SFE measures the fraction of the initial cloud gas mass that is converted into stars. We calculate the instantaneous SFE as Myers et al. (1986) using $\mathrm{SFE} = \mathrm{m_\star N_{YSO}}/(\mathrm{M_{gas}} + \mathrm{m_\star N_{YSO}})$, where M_{gas} is the total cloud gas mass we observe today and $m_\star$ is the average mass for a typical IMF (0,5 $\mathrm{M_\odot}$). Although different SFE values should be expected for different areas enclosing the cloud, we observe little variation. For the total area of the cloud ($w \leq 0{,}63$ pc) we find SFE = 0,0035. Alternatively, for eleven N(H_2) contour levels spanning from 0.08 to $1\times10^{23}\mathrm{cm}^{-2}$, the SFE varies between 0.0028 and 0.0034. It can be argued that the most correct estimation for the SFE is the one that covers the total area of the cloud. For that reason, we report SFE = 0.0035 corresponding to the area within $w < 0{,}63$ pc.

This result is an order of 10× lower than the median value SFE = 0.038 of molecular clouds (Megeath et al., 2022), and similarly lower to the SFE = 0,03 of the Orion A cloud (Megeath et al., 2016). However, we must account for the incompleteness when comparing structures at different distances and from different surveys. In particular, we have calibrated a correction factor $k = 5$ to compare G351 to Orion A (see above Section 5.1), which we apply to N_{YSO}. When corrected, we find SFE = 0,017, which is still ($\sim 2\times$) lower than that of Orion A. Furthermore, we probe the less evolved filament portion MF-north. Within $w \leq 0{,}63$ pc we have 33 dusty YSOs, and a gas mass of M = 5450 $\mathrm{M_\odot}$, so a low SFE= 0,003. Given the high mass and high line-mass of

G351, this low efficiency might be attributed to a very early evolutionary stage (see above). Magnetohydrodynamic (MHD) simulations of Grudić et al. (2019) show that the instantaneous SFE continuously increases after the first sink particle forms. Stellar feedback eventually halts the increase and the SFE remains constant at this high value.

On the other hand, the SFR measures the amount of solar masses that are converted into stars per unit time. We calculate it using SFR$= m_\star \frac{N_{YSO}}{t_{YSO}}$. When N_{YSO} is the number of protostars and disks, $t_{YSO} = 2{,}5$ Myr because it is the expected lifetime of the disks (after which the disk disappears, Megeath et al. 2022). Alternatively, when N_{YSO} is the number of protostars only, $t_{YSO} = 0{,}5$ Myr because it is the average lifetime of protostars (Dunham et al., 2014). Our YSO sample includes protostars, disks, and unclassified YSOs ($N_{YSO} = 68$ for $w < 0{,}63$ pc), hence we adopted $t_{YSO} =$ 2,5 Myr to estimate SFR = 13.6 $M_\odot\,\mathrm{Myr}^{-1}$ for the G351 filament. This value is much lower than the 715 $M_\odot\,\mathrm{Myr}^{-1}$ of Orion A (Lada et al., 2010) and only comparable to the 16 $M_\odot\,\mathrm{Myr}^{-1}$ found by Retes-Romero et al. (2017) for the cloud with the lowest SFR of their sample. Finally, we probe the less evolved MF-north. Within $w \leq 0{,}63$ pc (33 dusty YSOs) it has SFR$= 6{,}6\ M_\odot$.

5.4. Probing local intracloud star forming relations

To confirm whether intracloud SF-relations demonstrate a unique, universal law they must be tested on different clouds. We probe the Pokhrel et al. (2021) relation by introducing G351 and measuring its respective $\varepsilon_{\rm ff}$. Based on the three fundamental measurements of area A, N_{YSO} and gas mass $M_{\rm gas}$ (the latter two enclosed by the given area) for different N(H_2) contour levels, we derived Σ_{SFR}, Σ_{gas} and $t_{\rm ff}$. We follow their same procedure described in Pokhrel et al. (2020), but we briefly describe it here for clarity. For a given contour, we have $\Sigma_{SFR} = \mathrm{SFR}/\mathrm{A}$, $\Sigma_{gas} = M_{gas}/A$, and $t_{\rm ff} = \sqrt{3\pi/32\,G\rho}$, where ρ is the volumetric density of the cloud assuming its mass is spherically distributed (see Hu et al. 2021 for a discussion of the influence of this

assumption over this relation). For the SFR they only considered protostars, hence they used $t_{YSO} = 0{,}5$ Myr. The practical form of this Pokhrel et al. (2021) relation is $\log \Sigma_{\rm SFR} = \log\left(\Sigma_{\rm gas}/t_{\rm ff}\right) + \log \varepsilon_{\rm ff}$, where $\varepsilon_{\rm ff}$ is the fraction of gas mass converted to stars per free-fall time.

For G351 we did not limit our sample to only protostars because not all the catalogs we retrieved YSOs from provide a classification. Instead, we used our entire sample of YSOs (Sections 2.1.1 and 2.1.2), which includes protostars and disks, and accordingly used $t_{YSO} = 2{,}5$ Myr. We selected similar contour levels for all the clouds, ranging from 0.82 to 4.82×10^{22} cm^{-2} in steps of 4×10^{21} cm^{-2}, and they were selected within the resolution limitations of our N(H_2) map. We also replicate the Orion A cloud and its two main sub structures (ISF and L1641), using the column density N(H_2) of Stutz and Gould (2016) for the mass measurements, together with the declination limits they defined for each structure. For the SFR calculations, we used the Spitzer Orion Survey YSOs and the protostars of Megeath et al. (2012, 2016) because it is the most complete catalog over that area and for consistency with all analysis throughout this section. We note that when using (an slightly updated version of) the protostars catalog that Pokhrel et al. (2021) used (Pokhrel 2023, priv. comm.), we very closely reproduce their Orion A profile, obtaining $\varepsilon_{\rm ff} = 0{,}0086$ (14 % lower than their $\varepsilon_{\rm ff} = 0{,}001$). For the ISF and L1641 individually we estimated $\varepsilon_{\rm ff} = 0{,}0064$ and $\varepsilon_{\rm ff} = 0{,}008$, respectively.

In Fig. 5.4.1 the 12 clouds of Pokhrel et al. (2021) are represented by their mean and dispersion. We also include here an scaled G351 profile that accounts for the YSO incompleteness relative to the Orion A clouds, where we increased $N_{\rm YSO}$ in the SFR term by our factor $k = 5$ (Section 5.2). We measured a 'raw' $\varepsilon_{\rm ff} = 0{,}00042$ for the G351 filament. Moreover, after completeness correction, $\varepsilon_{\rm ff} = 0{,}002$. This value is lower than both the mean intracloud relation by a factor of 12 and that of the lowest cloud (Orion A) in the Pokhrel et al. (2021) sample by a factor of $\sim 4{,}7$. To obtain the latter values we averaged over the entire filament structure, but it is also informative to probe the less evolved north component (i.e. MF-north, Section 5.2) that contains the most quiescent

clumps (Leurini et al., 2019). This portion of the MF shows a lower $\varepsilon_{\rm ff}$ (= 0,0003) relative to G351 as a whole by a factor of $\sim$0.7. This highlights a significant difference in evolutionary stages throughout different environments within the G351 filament.

Our analysis demonstrates that the global star-forming activity in the G351 filament is low. To explain this we can argue a couple of potential reasons. First, the cloud may be less than 2.5 Myr in age, which would also result in an underestimate of the SFR, but would predict an elevated number of protostars compared to the more evolved pre-main sequence stars (e.g. Stutz and Kainulainen 2015, see models in Megeath et al. 2022). For the youngest clump in the MF, Giannetti et al. (2019) measured an age $\leq 10^5$ yr from mm-wave emission of chemical tracers. Second, the lower $\varepsilon_{\rm ff}$ might indicate that it varies with environment in our Galaxy. Third, mechanisms like B-fields or turbulence might be supporting the cloud against collapse. However, this last possibility, that of turbulence, would imply high line-widths to support the mass, line-mass, and volume densities calculated above. Moreover, the observation from Giannetti et al. (2019) that at least 'Clump 7' is sub-virial based on APEX observations of o-H_2D^+ ($1_{1,0} - 1_{1,1}$) line widths may further call into question large contributions of turbulent support at least on the scales of clumps. Moreover, as discussed above, the Ryabukhina and Zinchenko (2021) M/L value (scaled to our distance) would imply a sub-virial (relative to radial collapse) filament, as opposed to the equilibrium values these authors tentatively infer. Indeed, as Ryabukhina and Zinchenko (2021) point out (along with a careful discussion of possible uncertainties), despite the measurement of radial near-equilibrium, the G351 filament is in fact observed to be fragmenting and collapsing right now. Lastly and for the $\varepsilon_{\rm ff}$ measurement in particular, the spherical assumption might have played a role as the gas distribution is elongated and more likely characterized by a cylindrical geometry (see above).

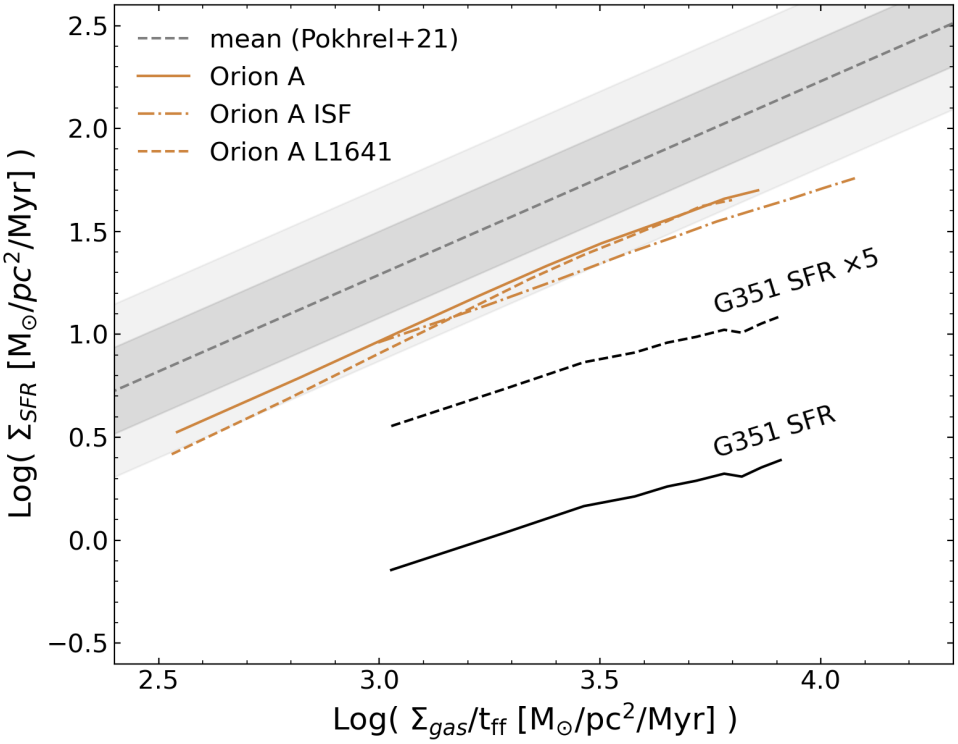

Figura 5.4.1: Grey-shaded area: SF-relation from Pokhrel et al. (2021), showing a linear-law where all clouds have a similar efficiency per free-fall time $\varepsilon_{\rm ff}$. Orange curves show Orion A and its sub-regions separately. When G351 is added to this diagram, the measured SFR implies a lower value of $\varepsilon_{\rm ff}$ than that of nearby clouds, even with our completeness correction $k = 5$.

Capítulo 6

Conclusions

We have characterized the global star forming properties of the G351 IRDC by systematically comparing to the Orion A cloud, and particularly the ISF, the best nearby reference for cluster formation in filaments. Based on the measurements of distance, gas mass, and YSO counts, we establish a solid comparative frame that allows us to (a) constrain its current star forming activity and (b) test intracloud SF- relations.

We first constrain the G351 distance following two Gaia DR3 based approaches. In method 1 we find sources clumping in proper motion space for only one narrow parallax range: $\varpi' \in [0{,}45, 0{,}50]$ mas. From that clump we estimate $D = 2{,}12 \pm 0{,}09$ kpc. In method 2 we consider YSOs that are Gaia-detected, and to maintain a relevant number of sources we probe the entire environment of G351. This field contains bright clouds that are plausibly associated to the filament, and in agreement with this association hypothesis we find that the YSOs clump in parallax. From that clump we estimate $D = 1{,}82 \pm 0{,}05$ kpc. As the two methods retrieve similar results we take their average and report the first Gaia-based distance to G351 $D = 2 \pm 0{,}15$ kpc, resolving at the same time the long-standing controversy about the G351 distance.

With this distance, we are then able to measure gas masses. We calculate mass from our column density N(H_2) map created from Herschel/APEX imaging. We first identify the

ridgeline of the filament, to then define its total length $L = 8{,}6$ pc, and conservatively define a total radial extent $w = 0{,}63$ pc, where w is the POS projected radius from the ridgeline of the filament. Within these dimensions there is an area of 11 pc^2 that encloses a total gas mass of 10 200 $M_\odot$. Beyond an absolute mass measurement, we focus on the − more comprehensive − distribution of the gas mass. We find that the G351 line-mass follows a simple power-law $\lambda = 1585(w/\mathrm{pc})^{0{,}62}\ M_\odot\,\mathrm{pc}^{-1}$, higher than that of all Orion A structures and California L1482 at all widths w where the profiles can be compared, except in the very center of the ONC (M42) at $w \leq 0{,}19$ pc. In particular, our λ is a factor of 3 greater than that of the ISF. In addition, we find that the power-law index $\gamma = 0{,}62$ of our λ profile is larger than all the Orion structures but similar to that of the California L1482 filament. All the above confirms that the G351 filament contains a concentrated reservoir of dense gas that has the potential to fuel active star formation.

In contrast, we measure a low star formation activity based on the YSOs found in the filament area. Our initial analysis of line YSO densities reveals that G351 is forming 5× fewer YSOs per parsec than the ISF, and when including mass, we find that the SFE is 1.8 times lower. For both results we consider the YSO incompleteness correction between G351 and the Orion A cloud (a factor of 5×). Additionally, by measuring SFRs (considering incompleteness) and gas masses per free-fall time we test star forming relations for local clouds. Here we measured a 'raw' $\varepsilon_{\mathrm{ff}} = 0{,}0004$ for the filament, which becomes $\varepsilon_{\mathrm{ff}} = 0{,}002$ after completeness correction. We show that the low star formation activity of this IRDC is significantly below the SF-relation of Pokhrel et al. (2021), with $> 2\sigma$ discrepancy from the mean local 12-cloud relation. Specifically, we measure a 1.1 dex lower $\varepsilon_{\mathrm{ff}}$ than the mean local intracloud SF-relation reported by Pokhrel et al. (2021), and a factor of 4.7 times lower than the least efficient cloud in that analysis, the Orion A cloud, which we also reproduce independently. This suggests that intracloud SF-relations do not capture the variations of properties of IRDCs relative to nearby star forming clouds.

Given its relatively large and concentrated reservoir of gas and hence its strikingly low star formation activity demonstrated here, this cloud begs for an explanation of what physical conditions produce such an inefficiency. One potential explanation is that G351 could be very young. However, it has already initiated cluster formation, so this hypothesis must be regarded with some caution unless one assumes rapid cluster formation or different ages of emergent start structures in the same maternal filament. Alternatively, it is possible that environmental mechanisms are supporting it against collapse, such as magnetic fields or turbulence. Regarding the latter, recent measurements of dense tracers in portions of the filament suggest it to be sub-virial (Giannetti et al., 2019; Ryabukhina and Zinchenko, 2021, scaling to our distance), hence turbulence appears a less likely candidate for supporting the cloud.

The low age hypothesis can be tested by further studies that identify the most embedded YSOs along the filament and in the active protocluster (e.g., using the James Webb Space Telescope), by measuring the ratio of the number of pre-main sequence stars with disks (Class II) to protostars (Class I) (Gutermuth et al., 2011; Stutz and Kainulainen, 2015; Megeath et al., 2022). We can further leverage high resolution ALMA detections of cores in the protocluster (Motte et al., 2022) and in the filament as a whole by determining the fraction of cores with protostars (Nony et al., 2023). This would establish their evolutionary stage, and in turn estimate their evolutionary timescales (albeit with small number statistics), calibrated to our current understanding of YSO and protostar lifetimes. Lastly, the magnetic field hypothesis should be tested with polarimetry. In particular, linear dust polarization is becoming increasingly observationally accessible (via e.g., ALMA, APEX, LCT, or CCAT-prime, to mention a few southern observatories that either have or will have polarization capabilities), and provides constraints on the geometry of the field, for example, that may depend on environment (main protocluster versus the rest of the filament).

Bibliografía

Álvarez-Gutiérrez, R. H., Stutz, A. M., Law, C. Y., Reissl, S., Klessen, R. S., Leigh, N. W. C., Liu, H. L., and Reeves, R. A. (2021). Filament Rotation in the California L1482 Cloud. , 908(1):86.

Benjamin, R. A., Churchwell, E., Babler, B. L., Bania, T. M., Clemens, D. P., Cohen, M., Dickey, J. M., Indebetouw, R., Jackson, J. M., Kobulnicky, H. A., Lazarian, A., Marston, A. P., Mathis, J. S., Meade, M. R., Seager, S., Stolovy, S. R., Watson, C., Whitney, B. A., Wolff, M. J., and Wolfire, M. G. (2003). Glimpse. i. an sirtf legacy project to map the inner galaxy. *Publications of the Astronomical Society of the Pacific*, 115(810):953.

Carey, S. J., Clark, F. O., Egan, M. P., Price, S. D., Shipman, R. F., and Kuchar, T. A. (1998). The Physical Properties of the Midcourse Space Experiment Galactic Infrared-dark Clouds. , 508(2):721–728.

Chen, X., Gan, C.-G., Ellingsen, S. P., He, J.-H., Shen, Z.-Q., and Titmarsh, A. (2013). Newly Identified Extended Green Objects (EGOs) from the Spitzer GLIMPSE II Survey. I. Catalog. , 206(1):9.

Churchwell, E., Babler, B. L., Meade, M. R., Whitney, B. A., Benjamin, R., Indebetouw, R., Cyganowski, C., Robitaille, T. P., Povich, M., Watson, C., and Bracker, S. (2009). The spitzer/glimpse surveys: A new view of the milky way. *Publications of the Astronomical Society of the Pacific*, 121(877):213.

Csengeri, T., Weiss, A., Wyrowski, F., Menten, K. M., Urquhart, J. S., Leurini, S., Schuller, F., Beuther, H., Bontemps, S., Bronfman, L., Henning, T., and Schneider, N. (2016). The ATLASGAL survey: distribution of cold dust in the Galactic plane. Combination with Planck data. , 585:A104.

Cunningham, N., Ginsburg, A., Galván-Madrid, R., Motte, F., Csengeri, T., Stutz, A. M., Fernández-López, M., Álvarez-Gutiérrez, R. H., Armante, M., Baug, T., Bonfand, M., Bontemps, S., Braine, J., Brouillet, N., Busquet, G., Díaz-González, D. J., Di Francesco, J., Gusdorf, A., Herpin, F., Liu, H., López-Sepulcre, A., Louvet, F., Lu, X., Maud, L., Nony, T., Olguin, F. A., Pouteau, Y., Rivera-Soto, R., Sandoval-Garrido, N. A., Sanhueza, P., Tatematsu, K., Towner, A. P. M., and Valeille-Manet, M. (2023). ALMA-IMF VII – First release of the full spectral line cubes:Core kinematics traced by DCN J=(3-2). *arXiv e-prints*, page arXiv:2306.14710.

Cutri, R. M., Wright, E. L., Conrow, T., Fowler, J. W., Eisenhardt, P. R. M., Grillmair,

C., Kirkpatrick, J. D., Masci, F., McCallon, H. L., Wheelock, S. L., Fajardo-Acosta, S., Yan, L., Benford, D., Harbut, M., Jarrett, T., Lake, S., Leisawitz, D., Ressler, M. E., Stanford, S. A., Tsai, C. W., Liu, F., Helou, G., Mainzer, A., Gettings, D., Gonzalez, A., Hoffman, D., Marsh, K. A., Padgett, D., Skrutskie, M. F., Beck, R. P., Papin, M., and Wittman, M. (2013). Explanatory Supplement to the AllWISE Data Release Products. Explanatory Supplement to the AllWISE Data Release Products, by R. M. Cutri et al.

Dunham, M. M., Stutz, A. M., Allen, L. E., Evans, N. J., I., Fischer, W. J., Megeath, S. T., Myers, P. C., Offner, S. S. R., Poteet, C. A., Tobin, J. J., and Vorobyov, E. I. (2014). The Evolution of Protostars: Insights from Ten Years of Infrared Surveys with Spitzer and Herschel. In Beuther, H., Klessen, R. S., Dullemond, C. P., and Henning, T., editors, *Protostars and Planets VI*, pages 195–218.

Egan, M. P., Shipman, R. F., Price, S. D., Carey, S. J., Clark, F. O., and Cohen, M. (1998). A Population of Cold Cores in the Galactic Plane. , 494(2):L199–L202.

Evans, N. J., Heiderman, A., and Vutisalchavakul, N. (2014). Star formation relations in nearby molecular clouds. *The Astrophysical Journal*, 782(2):114.

Forster, J. R. and Caswell, J. L. (1989). The spatial relationship of OH and H2O masers. , 213:339–350.

Gaia Collaboration, Prusti, T., de Bruijne, J. H. J., Brown, A. G. A., Vallenari, A., Babusiaux, C., Bailer-Jones, C. A. L., Bastian, U., Biermann, M., Evans, D. W., Eyer, L., Jansen, F., Jordi, C., Klioner, S. A., Lammers, U., Lindegren, L., Luri, X., Mignard, F., Milligan, D. J., Panem, C., Poinsignon, V., Pourbaix, D., Randich, S., Sarri, G., Sartoretti, P., Siddiqui, H. I., Soubiran, C., Valette, V., van Leeuwen, F., Walton, N. A., Aerts, C., Arenou, F., Cropper, M., Drimmel, R., Høg, E., Katz, D., Lattanzi, M. G., O'Mullane, W., Grebel, E. K., Holland, A. D., Huc, C., Passot, X., Bramante, L., Cacciari, C., Castañeda, J., Chaoul, L., Cheek, N., De Angeli, F., Fabricius, C., Guerra, R., Hernández, J., Jean-Antoine-Piccolo, A., Masana, E., Messineo, R., Mowlavi, N., Nienartowicz, K., Ordóñez-Blanco, D., Panuzzo, P., Portell, J., Richards, P. J., Riello, M., Seabroke, G. M., Tanga, P., Thévenin, F., Torra, J., Els, S. G., Gracia-Abril, G., Comoretto, G., Garcia-Reinaldos, M., Lock, T., Mercier, E., Altmann, M., Andrae, R., Astraatmadja, T. L., Bellas-Velidis, I., Benson, K., Berthier, J., Blomme, R., Busso, G., Carry, B., Cellino, A., Clementini, G., Cowell, S., Creevey, O., Cuypers, J., Davidson, M., De Ridder, J., de Torres, A., Delchambre, L., Dell'Oro, A., Ducourant, C., Frémat, Y., García-Torres, M., Gosset, E., Halbwachs, J. L., Hambly, N. C., Harrison, D. L., Hauser, M., Hestroffer, D., Hodgkin, S. T., Huckle, H. E., Hutton, A., Jasniewicz, G., Jordan, S., Kontizas, M., Korn, A. J., Lanzafame, A. C., Manteiga, M., Moitinho, A., Muinonen, K., Osinde, J., Pancino, E., Pauwels, T., Petit, J. M., Recio-Blanco, A., Robin, A. C., Sarro, L. M., Siopis, C., Smith, M., Smith, K. W., Sozzetti, A., Thuillot, W., van Reeven, W., Viala, Y., Abbas, U., Abreu Aramburu, A., Accart, S., Aguado, J. J., Allan, P. M., Allasia, W., Altavilla, G., Álvarez, M. A., Alves, J., Anderson, R. I., Andrei, A. H., Anglada Varela, E., Antiche, E., Antoja, T., Antón, S., Arcay, B., Atzei, A., Ayache, L., Bach, N., Baker, S. G., Balaguer-Núñez, L., Barache, C., Barata, C.,

Barbier, A., Barblan, F., Baroni, M., Barrado y Navascués, D., Barros, M., Barstow, M. A., Becciani, U., Bellazzini, M., Bellei, G., Bello García, A., Belokurov, V., Bendjoya, P., Berihuete, A., Bianchi, L., Bienaymé, O., Billebaud, F., Blagorodnova, N., Blanco-Cuaresma, S., Boch, T., Bombrun, A., Borrachero, R., Bouquillon, S., Bourda, G., Bouy, H., Bragaglia, A., Breddels, M. A., Brouillet, N., Brüsemeister, T., Bucciarelli, B., Budnik, F., Burgess, P., Burgon, R., Burlacu, A., Busonero, D., Buzzi, R., Caffau, E., Cambras, J., Campbell, H., Cancelliere, R., Cantat-Gaudin, T., Carlucci, T., Carrasco, J. M., Castellani, M., Charlot, P., Charnas, J., Charvet, P., Chassat, F., Chiavassa, A., Clotet, M., Cocozza, G., Collins, R. S., Collins, P., Costigan, G., Crifo, F., Cross, N. J. G., Crosta, M., Crowley, C., Dafonte, C., Damerdji, Y., Dapergolas, A., David, P., David, M., De Cat, P., de Felice, F., de Laverny, P., De Luise, F., De March, R., de Martino, D., de Souza, R., Debosscher, J., del Pozo, E., Delbo, M., Delgado, A., Delgado, H. E., di Marco, F., Di Matteo, P., Diakite, S., Distefano, E., Dolding, C., Dos Anjos, S., Drazinos, P., Durán, J., Dzigan, Y., Ecale, E., Edvardsson, B., Enke, H., Erdmann, M., Escolar, D., Espina, M., Evans, N. W., Eynard Bontemps, G., Fabre, C., Fabrizio, M., Faigler, S., Falcão, A. J., Farràs Casas, M., Faye, F., Federici, L., Fedorets, G., Fernández-Hernández, J., Fernique, P., Fienga, A., Figueras, F., Filippi, F., Findeisen, K., Fonti, A., Fouesneau, M., Fraile, E., Fraser, M., Fuchs, J., Furnell, R., Gai, M., Galleti, S., Galluccio, L., Garabato, D., García-Sedano, F., Garé, P., Garofalo, A., Garralda, N., Gavras, P., Gerssen, J., Geyer, R., Gilmore, G., Girona, S., Giuffrida, G., Gomes, M., González-Marcos, A., González-Núñez, J., González-Vidal, J. J., Granvik, M., Guerrier, A., Guillout, P., Guiraud, J., Gúrpide, A., Gutiérrez-Sánchez, R., Guy, L. P., Haigron, R., Hatzidimitriou, D., Haywood, M., Heiter, U., Helmi, A., Hobbs, D., Hofmann, W., Holl, B., Holland, G., Hunt, J. A. S., Hypki, A., Icardi, V., Irwin, M., Jevardat de Fombelle, G., Jofré, P., Jonker, P. G., Jorissen, A., Julbe, F., Karampelas, A., Kochoska, A., Kohley, R., Kolenberg, K., Kontizas, E., Koposov, S. E., Kordopatis, G., Koubsky, P., Kowalczyk, A., Krone-Martins, A., Kudryashova, M., Kull, I., Bachchan, R. K., Lacoste-Seris, F., Lanza, A. F., Lavigne, J. B., Le Poncin-Lafitte, C., Lebreton, Y., Lebzelter, T., Leccia, S., Leclerc, N., Lecoeur-Taibi, I., Lemaitre, V., Lenhardt, H., Leroux, F., Liao, S., Licata, E., Lindstrøm, H. E. P., Lister, T. A., Livanou, E., Lobel, A., Löffler, W., López, M., Lopez-Lozano, A., Lorenz, D., Loureiro, T., MacDonald, I., Magalhães Fernandes, T., Managau, S., Mann, R. G., Mantelet, G., Marchal, O., Marchant, J. M., Marconi, M., Marie, J., Marinoni, S., Marrese, P. M., Marschalkó, G., Marshall, D. J., Martín-Fleitas, J. M., Martino, M., Mary, N., Matijevič, G., Mazeh, T., McMillan, P. J., Messina, S., Mestre, A., Michalik, D., Millar, N. R., Miranda, B. M. H., Molina, D., Molinaro, R., Molinaro, M., Molnár, L., Moniez, M., Montegriffo, P., Monteiro, D., Mor, R., Mora, A., Morbidelli, R., Morel, T., Morgenthaler, S., Morley, T., Morris, D., Mulone, A. F., Muraveva, T., Musella, I., Narbonne, J., Nelemans, G., Nicastro, L., Noval, L., Ordénovic, C., Ordieres-Meré, J., Osborne, P., Pagani, C., Pagano, I., Pailler, F., Palacin, H., Palaversa, L., Parsons, P., Paulsen, T., Pecoraro, M., Pedrosa, R., Pentikäinen, H., Pereira, J., Pichon, B., Piersimoni, A. M., Pineau, F. X., Plachy, E., Plum, G., Poujoulet, E., Prša, A., Pulone, L., Ragaini, S., Rago, S., Rambaux, N., Ramos-Lerate, M., Ranalli, P., Rauw, G., Read, A., Regibo, S., Renk, F., Reylé, C., Ribeiro, R. A., Rimoldini, L., Ripepi, V., Riva, A., Rixon, G.,

Roelens, M., Romero-Gómez, M., Rowell, N., Royer, F., Rudolph, A., Ruiz-Dern, L., Sadowski, G., Sagristà Sellés, T., Sahlmann, J., Salgado, J., Salguero, E., Sarasso, M., Savietto, H., Schnorhk, A., Schultheis, M., Sciacca, E., Segol, M., Segovia, J. C., Segransan, D., Serpell, E., Shih, I. C., Smareglia, R., Smart, R. L., Smith, C., Solano, E., Solitro, F., Sordo, R., Soria Nieto, S., Souchay, J., Spagna, A., Spoto, F., Stampa, U., Steele, I. A., Steidelmüller, H., Stephenson, C. A., Stoev, H., Suess, F. F., Süveges, M., Surdej, J., Szabados, L., Szegedi-Elek, E., Tapiador, D., Taris, F., Tauran, G., Taylor, M. B., Teixeira, R., Terrett, D., Tingley, B., Trager, S. C., Turon, C., Ulla, A., Utrilla, E., Valentini, G., van Elteren, A., Van Hemelryck, E., van Leeuwen, M., Varadi, M., Vecchiato, A., Veljanoski, J., Via, T., Vicente, D., Vogt, S., Voss, H., Votruba, V., Voutsinas, S., Walmsley, G., Weiler, M., Weingrill, K., Werner, D., Wevers, T., Whitehead, G., Wyrzykowski, Ł., Yoldas, A., Žerjal, M., Zucker, S., Zurbach, C., Zwitter, T., Alecu, A., Allen, M., Allende Prieto, C., Amorim, A., Anglada-Escudé, G., Arsenijevic, V., Azaz, S., Balm, P., Beck, M., Bernstein, H. H., Bigot, L., Bijaoui, A., Blasco, C., Bonfigli, M., Bono, G., Boudreault, S., Bressan, A., Brown, S., Brunet, P. M., Bunclark, P., Buonanno, R., Butkevich, A. G., Carret, C., Carrion, C., Chemin, L., Chéreau, F., Corcione, L., Darmigny, E., de Boer, K. S., de Teodoro, P., de Zeeuw, P. T., Delle Luche, C., Domingues, C. D., Dubath, P., Fodor, F., Frézouls, B., Fries, A., Fustes, D., Fyfe, D., Gallardo, E., Gallegos, J., Gardiol, D., Gebran, M., Gomboc, A., Gómez, A., Grux, E., Gueguen, A., Heyrovsky, A., Hoar, J., Iannicola, G., Isasi Parache, Y., Janotto, A. M., Joliet, E., Jonckheere, A., Keil, R., Kim, D. W., Klagyivik, P., Klar, J., Knude, J., Kochukhov, O., Kolka, I., Kos, J., Kutka, A., Lainey, V., LeBouquin, D., Liu, C., Loreggia, D., Makarov, V. V., Marseille, M. G., Martayan, C., Martinez-Rubi, O., Massart, B., Meynadier, F., Mignot, S., Munari, U., Nguyen, A. T., Nordlander, T., Ocvirk, P., O'Flaherty, K. S., Olias Sanz, A., Ortiz, P., Osorio, J., Oszkiewicz, D., Ouzounis, A., Palmer, M., Park, P., Pasquato, E., Peltzer, C., Peralta, J., Péturaud, F., Pieniluoma, T., Pigozzi, E., Poels, J., Prat, G., Prod'homme, T., Raison, F., Rebordao, J. M., Risquez, D., Rocca-Volmerange, B., Rosen, S., Ruiz-Fuertes, M. I., Russo, F., Sembay, S., Serraller Vizcaino, I., Short, A., Siebert, A., Silva, H., Sinachopoulos, D., Slezak, E., Soffel, M., Sosnowska, D., Straižys, V., ter Linden, M., Terrell, D., Theil, S., Tiede, C., Troisi, L., Tsalmantza, P., Tur, D., Vaccari, M., Vachier, F., Valles, P., Van Hamme, W., Veltz, L., Virtanen, J., Wallut, J. M., Wichmann, R., Wilkinson, M. I., Ziaeepour, H., and Zschocke, S. (2016). The Gaia mission. , 595:A1.

Gaia Collaboration, Vallenari, A., Brown, A. G. A., Prusti, T., de Bruijne, J. H. J., Arenou, F., Babusiaux, C., Biermann, M., Creevey, O. L., Ducourant, C., Evans, D. W., Eyer, L., Guerra, R., Hutton, A., Jordi, C., Klioner, S. A., Lammers, U. L., Lindegren, L., Luri, X., Mignard, F., Panem, C., Pourbaix, D., Randich, S., Sartoretti, P., Soubiran, C., Tanga, P., Walton, N. A., Bailer-Jones, C. A. L., Bastian, U., Drimmel, R., Jansen, F., Katz, D., Lattanzi, M. G., van Leeuwen, F., Bakker, J., Cacciari, C., Castañeda, J., De Angeli, F., Fabricius, C., Fouesneau, M., Frémat, Y., Galluccio, L., Guerrier, A., Heiter, U., Masana, E., Messineo, R., Mowlavi, N., Nicolas, C., Nienartowicz, K., Pailler, F., Panuzzo, P., Riclet, F., Roux, W., Seabroke, G. M., Sordoørcit, R., Thévenin, F., Gracia-Abril, G., Portell, J., Teyssier, D., Altmann, M., Andrae, R., Audard, M., Bellas-Velidis, I., Benson, K., Berthier, J., Blomme, R.,

Burgess, P. W., Busonero, D., Busso, G., Cánovas, H., Carry, B., Cellino, A., Cheek, N., Clementini, G., Damerdji, Y., Davidson, M., de Teodoro, P., Nuñez Campos, M., Delchambre, L., Dell'Oro, A., Esquej, P., Fernández-Hernández, J., Fraile, E., Garabato, D., García-Lario, P., Gosset, E., Haigron, R., Halbwachs, J. L., Hambly, N. C., Harrison, D. L., Hernández, J., Hestroffer, D., Hodgkin, S. T., Holl, B., Janßen, K., Jevardat de Fombelle, G., Jordan, S., Krone-Martins, A., Lanzafame, A. C., Löffler, W., Marchal, O., Marrese, P. M., Moitinho, A., Muinonen, K., Osborne, P., Pancino, E., Pauwels, T., Recio-Blanco, A., Reylé, C., Riello, M., Rimoldini, L., Roegiers, T., Rybizki, J., Sarro, L. M., Siopis, C., Smith, M., Sozzetti, A., Utrilla, E., van Leeuwen, M., Abbas, U., Ábrahám, P., Abreu Aramburu, A., Aerts, C., Aguado, J. J., Ajaj, M., Aldea-Montero, F., Altavilla, G., Álvarez, M. A., Alves, J., Anders, F., Anderson, R. I., Anglada Varela, E., Antoja, T., Baines, D., Baker, S. G., Balaguer-Núñez, L., Balbinot, E., Balog, Z., Barache, C., Barbato, D., Barros, M., Barstow, M. A., Bartolomé, S., Bassilana, J. L., Bauchet, N., Becciani, U., Bellazzini, M., Berihuete, A., Bernet, M., Bertone, S., Bianchi, L., Binnenfeld, A., Blanco-Cuaresma, S., Blazere, A., Boch, T., Bombrun, A., Bossini, D., Bouquillon, S., Bragaglia, A., Bramante, L., Breedt, E., Bressan, A., Brouillet, N., Brugaletta, E., Bucciarelli, B., Burlacu, A., Butkevich, A. G., Buzzi, R., Caffau, E., Cancelliere, R., Cantat-Gaudin, T., Carballo, R., Carlucci, T., Carnerero, M. I., Carrasco, J. M., Casamiquela, L., Castellani, M., Castro-Ginard, A., Chaoul, L., Charlot, P., Chemin, L., Chiaramida, V., Chiavassa, A., Chornay, N., Comoretto, G., Contursi, G., Cooper, W. J., Cornez, T., Cowell, S., Crifo, F., Cropper, M., Crosta, M., Crowley, C., Dafonte, C., Dapergolas, A., David, M., David, P., de Laverny, P., De Luise, F., De March, R., De Ridder, J., de Souza, R., de Torres, A., del Peloso, E. F., del Pozo, E., Delbo, M., Delgado, A., Delisle, J. B., Demouchy, C., Dharmawardena, T. E., Di Matteo, P., Diakite, S., Diener, C., Distefano, E., Dolding, C., Edvardsson, B., Enke, H., Fabre, C., Fabrizio, M., Faigler, S., Fedorets, G., Fernique, P., Fienga, A., Figueras, F., Fournier, Y., Fouron, C., Fragkoudi, F., Gai, M., Garcia-Gutierrez, A., Garcia-Reinaldos, M., García-Torres, M., Garofalo, A., Gavel, A., Gavras, P., Gerlach, E., Geyer, R., Giacobbe, P., Gilmore, G., Girona, S., Giuffrida, G., Gomel, R., Gomez, A., González-Núñez, J., González-Santamaría, I., González-Vidal, J. J., Granvik, M., Guillout, P., Guiraud, J., Gutiérrez-Sánchez, R., Guy, L. P., Hatzidimitriou, D., Hauser, M., Haywood, M., Helmer, A., Helmi, A., Sarmiento, M. H., Hidalgo, S. L., Hilger, T., Hładczuk, N., Hobbs, D., Holland, G., Huckle, H. E., Jardine, K., Jasniewicz, G., Jean-Antoine Piccolo, A., Jiménez-Arranz, Ó., Jorissen, A., Juaristi Campillo, J., Julbe, F., Karbevska, L., Kervella, P., Khanna, S., Kontizas, M., Kordopatis, G., Korn, A. J., Kóspál, Á., Kostrzewa-Rutkowska, Z., Kruszyńska, K., Kun, M., Laizeau, P., Lambert, S., Lanza, A. F., Lasne, Y., Le Campion, J. F., Lebreton, Y., Lebzelter, T., Leccia, S., Leclerc, N., Lecoeur-Taibi, I., Liao, S., Licata, E. L., Lindstrøm, H. E. P., Lister, T. A., Livanou, E., Lobel, A., Lorca, A., Loup, C., Madrero Pardo, P., Magdaleno Romeo, A., Managau, S., Mann, R. G., Manteiga, M., Marchant, J. M., Marconi, M., Marcos, J., Marcos Santos, M. M. S., Marín Pina, D., Marinoni, S., Marocco, F., Marshall, D. J., Polo, L. M., Martín-Fleitas, J. M., Marton, G., Mary, N., Masip, A., Massari, D., Mastrobuono-Battisti, A., Mazeh, T., McMillan, P. J., Messina, S., Michalik, D., Millar, N. R., Mints, A., Molina, D., Molinaro, R., Molnár,

L., Monari, G., Monguió, M., Montegriffo, P., Montero, A., Mor, R., Mora, A., Morbidelli, R., Morel, T., Morris, D., Muraveva, T., Murphy, C. P., Musella, I., Nagy, Z., Noval, L., Ocaña, F., Ogden, A., Ordenovic, C., Osinde, J. O., Pagani, C., Pagano, I., Palaversa, L., Palicio, P. A., Pallas-Quintela, L., Panahi, A., Payne-Wardenaar, S., Peñalosa Esteller, X., Penttilä, A., Pichon, B., Piersimoni, A. M., Pineau, F. X., Plachy, E., Plum, G., Poggio, E., Prša, A., Pulone, L., Racero, E., Ragaini, S., Rainer, M., Raiteri, C. M., Rambaux, N., Ramos, P., Ramos-Lerate, M., Re Fiorentin, P., Regibo, S., Richards, P. J., Rios Diaz, C., Ripepi, V., Riva, A., Rix, H. W., Rixon, G., Robichon, N., Robin, A. C., Robin, C., Roelens, M., Rogues, H. R. O., Rohrbasser, L., Romero-Gómez, M., Rowell, N., Royer, F., Ruz Mieres, D., Rybicki, K. A., Sadowski, G., Sáez Núñez, A., Sagristà Sellés, A., Sahlmann, J., Salguero, E., Samaras, N., Sanchez Gimenez, V., Sanna, N., Santoveña, R., Sarasso, M., Schultheis, M., Sciacca, E., Segol, M., Segovia, J. C., Ségransan, D., Semeux, D., Shahaf, S., Siddiqui, H. I., Siebert, A., Siltala, L., Silvelo, A., Slezak, E., Slezak, I., Smart, R. L., Snaith, O. N., Solano, E., Solitro, F., Souami, D., Souchay, J., Spagna, A., Spina, L., Spoto, F., Steele, I. A., Steidelmüller, H., Stephenson, C. A., Süveges, M., Surdej, J., Szabados, L., Szegedi-Elek, E., Taris, F., Taylo, M. B., Teixeira, R., Tolomei, L., Tonello, N., Torra, F., Torra, J., Torralba Elipe, G., Trabucchi, M., Tsounis, A. T., Turon, C., Ulla, A., Unger, N., Vaillant, M. V., van Dillen, E., van Reeven, W., Vanel, O., Vecchiato, A., Viala, Y., Vicente, D., Voutsinas, S., Weiler, M., Wevers, T., Wyrzykowski, L., Yoldas, A., Yvard, P., Zhao, H., Zorec, J., Zucker, S., and Zwitter, T. (2022). Gaia Data Release 3: Summary of the content and survey properties. *arXiv e-prints*, page arXiv:2208.00211.

Giannetti, A., Bovino, S., Caselli, P., Leurini, S., Schleicher, D. R. G., Körtgen, B., Menten, K. M., Pillai, T., and Wyrowski, F. (2019). A timeline for massive star-forming regions via combined observation of o-H_2D^+ and N_2D^+. , 621:L7.

Ginsburg, A., Csengeri, T., Galván-Madrid, R., Cunningham, N., Álvarez-Gutiérrez, R. H., Baug, T., Bonfand, M., Bontemps, S., Busquet, G., Díaz-González, D. J., Fernández-López, M., Guzmán, A., Herpin, F., Liu, H., López-Sepulcre, A., Louvet, F., Maud, L., Motte, F., Nakamura, F., Nony, T., Olguin, F. A., Pouteau, Y., Sanhueza, P., Stutz, A. M., Towner, A. P. M., ALMA-IMF Consortium, Armante, M., Battersby, C., Bronfman, L., Braine, J., Brouillet, N., Chapillon, E., Di Francesco, J., Gusdorf, A., Izumi, N., Joncour, I., Walker Lu, X., Men'shchikov, A., Menten, K. M., Moraux, E., Molet, J., Mundy, L., Nguyen Luong, Q., Reyes-Reyes, S. D., Robitaille, J., Rosolowsky, E., Sandoval-Garrido, N. A., Svoboda, B., Tatematsu, K., Walker, D. L., Whitworth, A., Wu, B., and Wyrowski, F. (2022). ALMA-IMF. II. Investigating the origin of stellar masses: Continuum images and data processing. , 662:A9.

González Lobos, V. and Stutz, A. M. (2019). Gas velocity structure of the Orion A integral-shaped filament. , 489(4):4771–4782.

Grudić, M. Y., Hopkins, P. F., Lee, E. J., Murray, N., Faucher-Giguère, C.-A., and Johnson, L. C. (2019). On the nature of variations in the measured star formation efficiency of molecular clouds. , 488(2):1501–1518.

Gutermuth, R. A., Megeath, S. T., Myers, P. C., Allen, L. E., Pipher, J. L., and Fazio,

G. G. (2009). A spitzer survey of young stellar clusters within one kiloparsec of the sun: Cluster core extraction and basic structural analysis. *The Astrophysical Journal Supplement Series*, 184(1):18.

Gutermuth, R. A., Megeath, S. T., Myers, P. C., Allen, L. E., Pipher, J. L., and Fazio, G. G. (2010). Erratum: "a spitzer survey of young stellar clusters within one kiloparsec of the sun: Cluster core extraction and basic structural analysis" (2009, apjs, 184, 18). *The Astrophysical Journal Supplement Series*, 189(2):352.

Gutermuth, R. A., Pipher, J. L., Megeath, S. T., Myers, P. C., Allen, L. E., and Allen, T. S. (2011). A correlation between surface densities of young stellar objects and gas in eight nearby molecular clouds. *The Astrophysical Journal*, 739(2):84.

Hildebrand, R. H. (1983). The determination of cloud masses and dust characteristics from submillimetre thermal emission. , 24:267–282.

Hu, Z., Krumholz, M. R., Federrath, C., Pokhrel, R., and Gutermuth, R. A. (2021). Reconstructing three-dimensional densities from two-dimensional observations of molecular gas. , 502(4):5997–6009.

Kainulainen, J., Stutz, A. M., Stanke, T., Abreu-Vicente, J., Beuther, H., Henning, T., Johnston, K. G., and Megeath, S. T. (2017). Resolving the fragmentation of high line-mass filaments with ALMA: the integral shaped filament in Orion A. , 600:A141.

Kauffmann, J., Bertoldi, F., Bourke, T. L., Evans, N. J., I., and Lee, C. W. (2008). MAMBO mapping of Spitzer c2d small clouds and cores. , 487(3):993–1017.

Kauffmann, J. and Pillai, T. (2010). How Many Infrared Dark Clouds Can form Massive Stars and Clusters? , 723(1):L7–L12.

Kounkel, M., Hartmann, L., Loinard, L., Ortiz-León, G. N., Mioduszewski, A. J., Rodríguez, L. F., Dzib, S. A., Torres, R. M., Pech, G., Galli, P. A. B., Rivera, J. L., Boden, A. F., Evans, Neal J., I., Briceño, C., and Tobin, J. J. (2017). The Gould's Belt Distances Survey (GOBELINS) II. Distances and Structure toward the Orion Molecular Clouds. , 834(2):142.

Kuhn, M. A., Benjamin, R. A., Zucker, C., Krone-Martins, A., de Souza, R. S., Castro-Ginard, A., Ishida, E. E. O., Povich, M. S., and Hillenbrand, L. A. (2021a). A high pitch angle structure in the Sagittarius Arm. , 651:L10.

Kuhn, M. A., de Souza, R. S., Krone-Martins, A., Castro-Ginard, A., Ishida, E. E. O., Povich, M. S., Hillenbrand, L. A., and COIN Collaboration (2021b). SPICY: The Spitzer/IRAC Candidate YSO Catalog for the Inner Galactic Midplane. , 254(2):33.

Lada, C. J., Lombardi, M., and Alves, J. F. (2009). The California Molecular Cloud. , 703(1):52–59.

Lada, C. J., Lombardi, M., and Alves, J. F. (2010). On the Star Formation Rates in Molecular Clouds. , 724(1):687–693.

Lada, C. J., Lombardi, M., Roman-Zuniga, C., Forbrich, J., and Alves, J. F. (2013).

Schmidt's conjecture and star formation in molecular clouds. *The Astrophysical Journal*, 778(2):133.

Launhardt, R., Stutz, A. M., Schmiedeke, A., Henning, T., Krause, O., Balog, Z., Beuther, H., Birkmann, S., Hennemann, M., Kainulainen, J., Khanzadyan, T., Linz, H., Lippok, N., Nielbock, M., Pitann, J., Ragan, S., Risacher, C., Schmalzl, M., Shirley, Y. L., Stecklum, B., Steinacker, J., and Tackenberg, J. (2013). The Earliest Phases of Star Formation (EPoS): a Herschel key project. The thermal structure of low-mass molecular cloud cores. , 551:A98.

Leurini, S., Codella, C., Zapata, L., Beltrán, M. T., Schilke, P., and Cesaroni, R. (2011a). On the kinematics of massive star forming regions: the case of IRAS 17233-3606. , 530:A12.

Leurini, S., Pillai, T., Stanke, T., Wyrowski, F., Testi, L., Schuller, F., Menten, K. M., and Thorwirth, S. (2011b). The molecular distribution of the IRDC G351.77-0.51. , 533:A85.

Leurini, S., Schisano, E., Pillai, T., Giannetti, A., Urquhart, J., Csengeri, T., Casu, S., Cunningham, M., Elia, D., Jones, P. A., König, C., Molinari, S., Stanke, T., Testi, L., Wyrowski, F., and Menten, K. M. (2019). Characterising the high-mass star forming filament G351.776-0.527 with Herschel and APEX dust continuum and gas observations. , 621:A130.

Li, S., Sanhueza, P., Zhang, Q., Guido, G., Sabatini, G., Morii, K., Lu, X., Tafoya, D., Nakamura, F., Izumi, N., Tatematsu, K., and Li, F. (2023). The ALMA Survey of 70 m Dark High-mass Clumps in Early Stages (ASHES). VIII. Dynamics of Embedded Dense Cores. *arXiv e-prints*, page arXiv:2304.01718.

Lindegren, L., Bastian, U., Biermann, M., Bombrun, A., de Torres, A., Gerlach, E., Geyer, R., Hernández, J., Hilger, T., Hobbs, D., Klioner, S. A., Lammers, U., McMillan, P. J., Ramos-Lerate, M., Steidelmüller, H., Stephenson, C. A., and van Leeuwen, F. (2021). Gaia Early Data Release 3. Parallax bias versus magnitude, colour, and position. , 649:A4.

MacLeod, G. C., Scalise, Eugenio, J., Saedt, S., Galt, J. A., and Gaylard, M. J. (1998). Masers in Massive Star-Forming Regions Associated with the Brightest Steep-Spectrum IRAS Point Sources. , 116(4):1897–1905.

Marton, G., Ábrahám, P., Szegedi-Elek, E., Varga, J., Kun, M., Kóspál, Á., Varga-Verebélyi, E., Hodgkin, S., Szabados, L., Beck, R., and Kiss, C. (2019). Identification of Young Stellar Object candidates in the Gaia DR2 x AllWISE catalogue with machine learning methods. , 487(2):2522–2537.

Megeath, S. T., Gutermuth, R., Muzerolle, J., Kryukova, E., Flaherty, K., Hora, J. L., Allen, L. E., Hartmann, L., Myers, P. C., Pipher, J. L., Stauffer, J., Young, E. T., and Fazio, G. G. (2012). The Spitzer Space Telescope Survey of the Orion A and B Molecular Clouds. I. A Census of Dusty Young Stellar Objects and a Study of Their Mid-infrared Variability. , 144(6):192.

Megeath, S. T., Gutermuth, R., Muzerolle, J., Kryukova, E., Hora, J. L., Allen, L. E., Flaherty, K., Hartmann, L., Myers, P. C., Pipher, J. L., Stauffer, J., Young, E. T., and Fazio, G. G. (2016). The Spitzer Space Telescope Survey of the Orion A and B Molecular Clouds. II. The Spatial Distribution and Demographics of Dusty Young Stellar Objects. , 151(1):5.

Megeath, S. T., Gutermuth, R. A., and Kounkel, M. A. (2022). Low mass stars as tracers of star and cluster formation. *Publications of the Astronomical Society of the Pacific*, 134(1034):042001.

Miettinen, O., Harju, J., Haikala, L. K., and Pomrén, C. (2006). SiO and CH_3CCH abundances and dust emission in high-mass star-forming cores. , 460(3):721–731.

Molinari, S., Schisano, E., Elia, D., Pestalozzi, M., Traficante, A., Pezzuto, S., Swinyard, B. M., Noriega-Crespo, A., Bally, J., Moore, T. J. T., Plume, R., Zavagno, A., di Giorgio, A. M., Liu, S. J., Pilbratt, G. L., Mottram, J. C., Russeil, D., Piazzo, L., Veneziani, M., Benedettini, M., Calzoletti, L., Faustini, F., Natoli, P., Piacentini, F., Merello, M., Palmese, A., Del Grande, R., Polychroni, D., Rygl, K. L. J., Polenta, G., Barlow, M. J., Bernard, J. P., Martin, P. G., Testi, L., Ali, B., André, P., Beltrán, M. T., Billot, N., Carey, S., Cesaroni, R., Compiègne, M., Eden, D., Fukui, Y., Garcia-Lario, P., Hoare, M. G., Huang, M., Joncas, G., Lim, T. L., Lord, S. D., Martinavarro-Armengol, S., Motte, F., Paladini, R., Paradis, D., Peretto, N., Robitaille, T., Schilke, P., Schneider, N., Schulz, B., Sibthorpe, B., Strafella, F., Thompson, M. A., Umana, G., Ward-Thompson, D., and Wyrowski, F. (2016). Hi-GAL, the Herschel infrared Galactic Plane Survey: photometric maps and compact source catalogues. First data release for the inner Milky Way: +68° $\geq$ l $\geq$ -70°. , 591:A149.

Molinari, S., Swinyard, B., Bally, J., Barlow, M., Bernard, J. P., Martin, P., Moore, T., Noriega-Crespo, A., Plume, R., Testi, L., Zavagno, A., Abergel, A., Ali, B., Anderson, L., André, P., Baluteau, J. P., Battersby, C., Beltrán, M. T., Benedettini, M., Billot, N., Blommaert, J., Bontemps, S., Boulanger, F., Brand, J., Brunt, C., Burton, M., Calzoletti, L., Carey, S., Caselli, P., Cesaroni, R., Cernicharo, J., Chakrabarti, S., Chrysostomou, A., Cohen, M., Compiegne, M., de Bernardis, P., de Gasperis, G., di Giorgio, A. M., Elia, D., Faustini, F., Flagey, N., Fukui, Y., Fuller, G. A., Ganga, K., Garcia-Lario, P., Glenn, J., Goldsmith, P. F., Griffin, M., Hoare, M., Huang, M., Ikhenaode, D., Joblin, C., Joncas, G., Juvela, M., Kirk, J. M., Lagache, G., Li, J. Z., Lim, T. L., Lord, S. D., Marengo, M., Marshall, D. J., Masi, S., Massi, F., Matsuura, M., Minier, V., Miville-Deschênes, M. A., Montier, L. A., Morgan, L., Motte, F., Mottram, J. C., Müller, T. G., Natoli, P., Neves, J., Olmi, L., Paladini, R., Paradis, D., Parsons, H., Peretto, N., Pestalozzi, M., Pezzuto, S., Piacentini, F., Piazzo, L., Polychroni, D., Pomarès, M., Popescu, C. C., Reach, W. T., Ristorcelli, I., Robitaille, J. F., Robitaille, T., Rodón, J. A., Roy, A., Royer, P., Russeil, D., Saraceno, P., Sauvage, M., Schilke, P., Schisano, E., Schneider, N., Schuller, F., Schulz, B., Sibthorpe, B., Smith, H. A., Smith, M. D., Spinoglio, L., Stamatellos, D., Strafella, F., Stringfellow, G. S., Sturm, E., Taylor, R., Thompson, M. A., Traficante, A., Tuffs, R. J., Umana, G., Valenziano, L., Vavrek, R., Veneziani, M., Viti, S., Waelkens, C., Ward-Thompson, D., White, G., Wilcock, L. A., Wyrowski, F., Yorke, H. W., and

Zhang, Q. (2010). Clouds, filaments, and protostars: The Herschel Hi-GAL Milky Way. , 518:L100.

Motte, F., Bontemps, S., Csengeri, T., Pouteau, Y., Louvet, F., Stutz, A. M., Cunningham, N., López-Sepulcre, A., Brouillet, N., Galván-Madrid, R., Ginsburg, A., Maud, L., Men'shchikov, A., Nakamura, F., Nony, T., Sanhueza, P., Álvarez-Gutiérrez, R. H., Armante, M., Baug, T., Bonfand, M., Busquet, G., Chapillon, E., Díaz-González, D., Fernández-López, M., Guzmán, A. E., Herpin, F., Liu, H. L., Olguin, F., Towner, A. P. M., Bally, J., Battersby, C., Braine, J., Bronfman, L., Chen, H. R. V., Dell'Ova, P., Di Francesco, J., González, M., Gusdorf, A., Hennebelle, P., Izumi, N., Joncour, I., Lee, Y. N., Lefloch, B., Lesaffre, P., Lu, X., Menten, K. M., Mignon-Risse, R., Molet, J., Moraux, E., Mundy, L., Nguyen Luong, Q., Reyes, N., Reyes Reyes, S. D., Robitaille, J. F., Rosolowsky, E., Sandoval-Garrido, N. A., Schuller, F., Svoboda, B., Tatematsu, K., Thomasson, B., Walker, D., Wu, B., Whitworth, A. P., and Wyrowski, F. (2022). ALMA-IMF. I. Investigating the origin of stellar masses: Introduction to the Large Program and first results. , 662:A8.

Motte, F., Bontemps, S., and Louvet, F. (2018). High-Mass Star and Massive Cluster Formation in the Milky Way. , 56:41–82.

Myers, P. C., Dame, T. M., Thaddeus, P., Cohen, R. S., Silverberg, R. F., Dwek, E., and Hauser, M. G. (1986). Molecular Clouds and Star Formation in the Inner Galaxy: A Comparison of CO, H ii, and Far-Infrared Surveys. , 301:398.

Nony, T., Galván-Madrid, R., Motte, F., Pouteau, Y., Cunningham, N., Louvet, F., Stutz, A. M., Lefloch, B., Bontemps, S., Brouillet, N., Ginsburg, A., Joncour, I., Herpin, F., Sanhueza, P., Csengeri, T., Towner, A. P. M., Bonfand, M., Fernández-López, M., Baug, T., Bronfman, L., Busquet, G., Di Francesco, J., Gusdorf, A., Lu, X., Olguin, F., Valeille-Manet, M., and Whitworth, A. P. (2023). ALMA-IMF. V. Prestellar and protostellar core populations in the W43 cloud complex. , 674:A75.

Norris, R. P., Whiteoak, J. B., Caswell, J. L., Wieringa, M. H., and Gough, R. G. (1993). Synthesis Images of 6.7 GHz Methanol Masers. , 412:222.

Ossenkopf, V. and Henning, T. (1994). Dust opacities for protostellar cores. , 291:943–959.

Pokhrel, R., Gutermuth, R. A., Betti, S. K., Offner, S. S. R., Myers, P. C., Megeath, S. T., Sokol, A. D., Ali, B., Allen, L., Allen, T. S., Dunham, M. M., Fischer, W. J., Henning, T., Heyer, M., Hora, J. L., Pipher, J. L., Tobin, J. J., and Wolk, S. J. (2020). Star–gas surface density correlations in 12 nearby molecular clouds. i. data collection and star-sampled analysis. *The Astrophysical Journal*, 896(1):60.

Pokhrel, R., Gutermuth, R. A., Krumholz, M. R., Federrath, C., Heyer, M., Khullar, S., Megeath, S. T., Myers, P. C., Offner, S. S. R., Pipher, J. L., Fischer, W. J., Henning, T., and Hora, J. L. (2021). The Single-cloud Star Formation Relation. , 912(1):L19.

Povich, M. S., Kuhn, M. A., Getman, K. V., Busk, H. A., Feigelson, E. D., Broos, P. S., Townsley, L. K., King, R. R., and Naylor, T. (2013). The MYStIX Infrared-Excess Source Catalog. , 209(2):31.

Rathborne, J. M., Simon, R., and Jackson, J. M. (2007). The Detection of Protostellar Condensations in Infrared Dark Cloud Cores. , 662(2):1082–1092.

Retes-Romero, R., Mayya, Y. D., Luna, A., and Carrasco, L. (2017). The star-formation law in galactic high-mass star-forming molecular clouds. *The Astrophysical Journal*, 839(2):113.

Ryabukhina, O. L. and Zinchenko, I. I. (2021). A multiline study of the filamentary infrared dark cloud G351.78-0.54. , 505(1):726–737.

Sadavoy, S. I., Stutz, A. M., Schnee, S., Mason, B. S., Di Francesco, J., and Friesen, R. K. (2016). Dust emissivity in the star-forming filament OMC 2/3. , 588:A30.

Sanhueza, P., Contreras, Y., Wu, B., Jackson, J. M., Guzmán, A. E., Zhang, Q., Li, S., Lu, X., Silva, A., Izumi, N., Liu, T., Miura, R. E., Tatematsu, K., Sakai, T., Beuther, H., Garay, G., Ohashi, S., Saito, M., Nakamura, F., Saigo, K., Veena, V. S., Nguyen-Luong, Q., and Tafoya, D. (2019). The ALMA Survey of 70 μm Dark High-mass Clumps in Early Stages (ASHES). I. Pilot Survey: Clump Fragmentation. , 886(2):102.

Sanhueza, P., Jackson, J. M., Foster, J. B., Garay, G., Silva, A., and Finn, S. C. (2012). Chemistry in Infrared Dark Cloud Clumps: A Molecular Line Survey at 3 mm. , 756(1):60.

Stutz, A. M. (2018). Slingshot mechanism for clusters: Gas density regulates star density in the Orion Nebula Cluster (M42). , 473(4):4890–4899.

Stutz, A. M., Gonzalez-Lobos, V., and Gould, A. (2018). Gaia: Orion's Integral Shaped Filament is a Standing Wave. *arXiv e-prints*, page arXiv:1807.11496.

Stutz, A. M. and Gould, A. (2016). Slingshot mechanism in Orion: Kinematic evidence for ejection of protostars by filaments. , 590:A2.

Stutz, A. M. and Kainulainen, J. (2015). Evolution of column density distributions within Orion A$\star$. , 577:L6.

Stutz, A. M., Tobin, J. J., Stanke, T., Megeath, S. T., Fischer, W. J., Robitaille, T., Henning, T., Ali, B., di Francesco, J., Furlan, E., Hartmann, L., Osorio, M., Wilson, T. L., Allen, L., Krause, O., and Manoj, P. (2013). A herschel* and apex census of the reddest sources in orion: Searching for the youngest protostars†. *The Astrophysical Journal*, 767(1):36.

Wright, E. L., Eisenhardt, P. R. M., Mainzer, A. K., Ressler, M. E., Cutri, R. M., Jarrett, T., Kirkpatrick, J. D., Padgett, D., McMillan, R. S., Skrutskie, M., Stanford, S. A., Cohen, M., Walker, R. G., Mather, J. C., Leisawitz, D., Gautier, Thomas N., I., McLean, I., Benford, D., Lonsdale, C. J., Blain, A., Mendez, B., Irace, W. R., Duval, V., Liu, F., Royer, D., Heinrichsen, I., Howard, J., Shannon, M., Kendall, M., Walsh, A. L., Larsen, M., Cardon, J. G., Schick, S., Schwalm, M., Abid, M., Fabinsky, B., Naes, L., and Tsai, C.-W. (2010). The Wide-field Infrared Survey Explorer (WISE): Mission Description and Initial On-orbit Performance. , 140(6):1868–1881.